Accepted Manuscript

Yuki Itoh and Mario Parente, "A new method for atmospheric correction and de-noising of CRISM hyperspectral data," Icarus, 2020.

https://doi.org/10.1016/j.icarus.2020.114024

© 2020. This manuscript version is made available under the Creative Commons "Attribution-NonCommercial-NoDerivatives 4.0 International" license (CC-BY-NC-ND 4.0) https://creativecommons.org/licenses/by-nc-nd/4.0/.

A new method for atmospheric correction and de-noising of CRISM hyperspectral data

Yuki Itoh[a,*], Mario Parente[a]

[a]*Department of Electrical and Computer Engineering, University of Massachusetts, Amherst*

Abstract

We propose a new method to perform atmospheric correction and de-noising on hyperspectral image cubes acquired by the Compact Reconnaissance Imaging Spectrometer for Mars (CRISM) on board NASA's Mars Reconnaissance Orbiter (MRO). The CRISM imager has had an important role in advancing our understanding of many aspects of Martian mineralogy. Many mineral detections from CRISM data have been facilitated by significant efforts in the development of the CRISM data processing pipeline to retrieve surface reflectance. However, some residuals remain in CRISM spectra after atmospheric correction, causing difficulty in the interpretation of processed reflectance spectra. In addition, CRISM images are occasionally corrupted with high noise levels exhibiting heterogeneous statistical properties. This paper identifies the cause of such spectral distortions and describe a technique that simultaneously performs both atmospheric correction and de-noising for each image cube individually. In particular, our method focuses on the 1.0-2.6 μm wavelength region of CRISM images and is applicable to images of non-icy surfaces. Experimental results show that our technique is able to significantly mitigate noise and distortions from various sources like gaseous absorptions, detector temperature, and water ice aerosols, compared with the atmospheric correction method in the CRISM official processing pipeline called volcano scan correction, for a variety of scenes. Careful validations that include the qualitative examination of noise and artifacts both on ratioed and non-ratioed spectra and comparison using multiple overlapping images strengthen confidence in our approach.

Keywords: Image Processing, Mars surface, Mars atmosphere, Spectroscopy, Infrared Observations

Accepted manuscript to Icarus, Elsevier

1. Introduction

1.1. Motivation

Since the beginning of its operations, the Compact Reconnaissance Imaging Spectrometer for Mars (CRISM) (Murchie et al., 2007) on board of Mars Reconnaissance Orbiter (MRO) has made significant contributions towards understanding many detailed aspects of the surface mineralogy of Mars thanks to its high spectral and spatial resolution. CRISM has reinforced and detailed previous findings made by OMEGA (Observatoire pour la Mineralogie, L'Eau, les Glaces et l'Activitié), such as the identification of phyllosilicates including kaolinite, montmorillonite, muscovite, illite, chlorite, saponite, nontronite, and hydrated silica (Poulet et al., 2005; Bibring et al., 2006; Mustard et al., 2008). Moreover, CRISM has confirmed the existence of opaline silica (Milliken et al., 2008) and Fe-Mg carbonate (Ehlmann et al., 2008b, 2009; Brown et al., 2010, 2020), two minerals that were not previously discovered. Many other minerals have been identified (Carter et al., 2015). Mineral detections are compiled and summarized in Viviano-Beck et al. (2014) and Ehlmann and Edwards (2014). More recently, mineral detections and mapping derived from CRISM images for Jezero crater (Ehlmann et al., 2008a,b, 2009; Goudge et al., 2015, 2017; Tarnas et al., 2019; Dundar et al., 2019; Horgan et al., 2020; Brown et al., 2020; Parente et al., 2019) are also expected to support the Perseverance rover mission (Williford et al., 2018) scheduled for launch in 2020.

Raw image cubes acquired by CRISM require complex processing protocols before they can be used for mineral identification (Murchie et al., 2007, 2009b, 2016). In the current pipeline for CRISM products, a raw image cube recorded in a 12-bit integer format undergoes calibration and corrections to be converted to an apparent reflectance, I/F image cube (Murchie et al., 2016). The I/F image is then processed to the TRR3 I/F product (TRR: Targeted Reduced Data Record), with TRR3 filtering using iterative kernel filter (IKF) and ratio shift correction (RSC) applied in order to remediate outstanding noise and

*Corresponding author
URL: yitoh@umass.edu (Yuki Itoh)

spatial stripes. Some data are further processed with photometric correction, atmospheric correction, repetitive filtering using RSC for de-spiking and de-striping, smile correction, and empirical geometric normalization. Finally, visible and near infrared (VNIR) and infrared (IR) images, are map projected and spectrally combined, producing the TER/MTRDR data, currently the most advanced products available for CRISM (TER:Targeted Empirical Data Record, non-map projected version and MTRDR: Map Projected Targeted Reduced Data Record) (Seelos et al., 2012, 2016; Murchie et al., 2016).

Artifacts still persist in the corrected I/F spectra as residuals of the atmospheric correction process. Other artifacts due to calibration errors can also be observed. Practitioners successfully abate systematic, column-dependent distortions by spectral ratioing (Mustard et al., 2005, 2008; Ehlmann et al., 2008b; Milliken et al., 2008; Ehlmann et al., 2009), i.e. by dividing the spectral signature of interest with a hopefully unremarkable spectrum in the same column. The division carries, however, the risk of changing the shape of the continuum of the spectrum that may cause the misinterpretation of spectral absorption features. Furthermore, spectral ratioing requires spatial averaging as the division always amplifies random noise. This complicates the identification of species in small deposits. Finally, the selection of unremarkable spectral denominators relies on a manual and subjective inspection by the individual user.

The so-called "volcano scan" correction, is the atmospheric compensation method currently used in the pipeline for CRISM IR images (Murchie et al., 2009a,b; Seelos et al., 2011, 2016). The technique was first proposed for atmospheric correction by the OMEGA team (Langevin et al., 2005; Mustard et al., 2005) and has been used to produce the CRISM TER and MTRDR data products. It assumes a Beer-Lambert model and uses empirical transmission spectra derived from the ratio of I/F spectra at the the summit and the base of Olympus Mons. The atmospheric contribution is removed by dividing each of the I/F spectra in the image by the empirically derived transmission spectra scaled appropriately by a factor estimated for each I/F spectrum. The volcano scan correction can be performed using the publicly available software, CRISM Analysis Toolkit (CAT). The latest version (currently 7.4) provides a better estimate of the scaling factor (McGuire et al., 2009), the

optimal selection of a transmission spectrum for each scene, and an empirical correction for a bowl-shape artifact around the 2.0 μm wavelength region (Morgan et al., 2011). While these modifications led to significant improvements in the quality of the signal, a considerable amount of distortions remains due to atmospheric absorptions and instrument artifacts. In addition, the set of available transmission spectra only partially models temporal and spatial variations of atmospheric conditions and thermally-induced random shifts of the central wavelength of the detectors.

The current calibration and correction pipeline for IR cubes was designed to operate at a range of IR detector temperatures much smaller than the ones recorded in a large set of scenes. As a result, CRISM IR images acquired at elevated IR detector temperatures, which already suffer from more severe noise and higher frequency of bad pixels, can exhibit problematic artifacts after calibration. In some cases, the current processing pipeline also causes the emergence of *spurious absorptions* occasionally in small outcrops due to TRR3 filtering on *spike clusters* regardless of IR detector temperature (Leask et al., 2018). Leask et al. (2018) showed that the detection of perchlorate (Ojha et al., 2015) is likely to be a false positive brought by such spurious absorptions.

This paper proposes a new method for simultaneous atmospheric correction and denoising of CRISM IR images over the 1.0-2.6 μm wavelength region. Our technique removes most of the residuals of the atmospheric correction endemic in the volcano scan method and mitigates the outstanding noise even in images acquired at elevated IR detector temperatures. The removal of systematic column-dependent artifacts, makes spectral ratioing unnecessary in most cases, which will expedite the analysis of images. Our method deals with the noise before TRR3 filtering is applied and artifacts originated from it will be avoided. The new method supports a wide range of scenes with non-icy surfaces, including ones whose atmospheric spectra include contributions from water ice aerosols.

Our proposed method extracts an atmospheric transmission spectrum directly from each image rather than estimating it from the atmospheric parameters using radiative transfer models. The underlying idea is that information regarding small static errors and time-varying and spatially-varying atmospheric gaseous absorptions detected at a certain instru-

ment temperature is encoded in the spectra of each CRISM image column. On the other hand, the extraction of the underlying atmospheric transmission spectrum from the image requires isolating the atmospheric contribution from surface contributions, which are unknown a priori. We address this issue by accurately modeling the surface reflectance using a modified version of the hyperspectral unmixing with adaptive background (Itoh and Parente, 2017b). We believe that our unmixing model is suitable since it is specifically designed for geological exploration where observed reflectance is expected to be mixed with smooth unremarkable spectra caused by dust and aerosols. In our algorithm, the surface mixing model and the transmission spectrum are estimated in an iterative way. A de-noising stage is also integrated, where large noise spikes are flagged and removed. This work includes significant improvements over our earlier efforts (Itoh and Parente, 2017a, 2018) and initial results were presented in Itoh and Parente (2019a).

1.2. Previous work

To improve upon the volcano-scan technique, atmospheric-correction approaches based on forward modeling of radiative transfer using discrete ordinate radiative transfer code (DISORT) have been proposed (McGuire et al., 2008; Smith et al., 2009; Wolff et al., 2009; Arvidson et al., 2014; Kreisch et al., 2017). Input atmospheric parameters are initialized/estimated from Martian climatological data measured by other instruments. This method also considers scattering and absorption by dust and water ice aerosols.

The presence of noise and artifacts in CRISM products have compelled the development of several de-noising approaches. For the previous iteration of CRISM targeted observations (TRR2), the CRISM Iterative Recognition and Removal of Unwanted Spiking (CIRRUS) (Parente, 2008) and a filtering based approach implemented within the mapping method proposed by Carter et al. (2013) were implemented. The major update of the CRISM targeted products to version 3 (TRR3) provided an improvement in calibration with the addition of TRR3 filtering (Seelos et al., 2009; Murchie et al., 2016). In this new era, a denoising method (Parente et al., 2014) and a Complement to CRISM Analysis Toolkit (CoTCAT) (Bultel et al., 2015) were proposed to complement the TRR3 filtering. More

recently, Kreisch et al. (2017) implemented a simultaneous de-noising and map-projecting method using a maximum likelihood for single scattering albedo obtained by DISORT under that assumption that noise follows a Poisson distribution, combining with prior processing using a median filter. He et al. (2019) advanced this idea by injecting hypothesis testing into maximum likelihood based de-noising method, which allows the automatic evaluation of noise distribution. Here, we employ a different approach altogether that simultaneously performs atmospheric correction and de-noising from in-scene spectra.

1.3. CRISM data

CRISM is a hyperspectral imager, observing the Martian surface at hundreds of narrow wavelength bands over the visible to infrared region. The instrument has two sets of spectrographs and detector focal planes, for the VNIR wavelength region (0.362-1.053 μm) and the IR wavelength region (1.002-3.920 μm), with their slit shared. The VNIR and IR image cubes are simultaneously recorded during acquisition. The pitch of the spectral channels is as good as 6.5 nm to achieve fine mineral identifications and a total of 107 bands for the VNIR and 438 bands for the IR are measured. CRISM has several observation modes with different spatial and spectral resolutions to achieve multiple research objectives.

In this study, we focus on image cubes acquired in the Full Targeted Resolution (FRT), the Half Resolution Long (HRL), the Half Resolution Short (HRS), the Full Resolution Short (FRS), or Along Track Oversampled (ATO) modes, where the imager operates with the highest spectral resolution. We focus on IR image cubes over 1.0-2.6 μm wavelength region. This wavelength region has been used for many mineral identifications in the literature, but we found that it is significantly affected by artifacts caused by the volcano scan method and occasionally by severe noise and other calibration errors. We note that our method cannot be directly expanded into other wavelength regions. For instance, applying our method to the longer wavelength region (2.8-4.0 μm) of CRISM IR images would require complementing it with the compensation of the thermal emission component. For the VNIR wavelength region, artifacts and noise corrected by our method are scarcely present, because of little atmospheric gaseous absorption over this range and a much lower noise level of the VNIR

detector.

2. CRISM noise and artifacts

This section investigates four major issues observed in the current CRISM products: 1) a systematic effect caused either by atmospheric distortions or within the calibration pipeline, 2) random noise, 3) interpolation bias, namely systematic spike trains created in the calibration pipeline, which is informally known as bed-of-nails, and 4) the spectral effect of water-ice aerosols. Here, we define an *image frame* as the image captured at the detector array at a time, spanning the cross-track and wavelength directions, and a *pixel* as an image cell in one image frame spanning the cross-track and wavelength dimensions. If the image is binned in the cross-track dimension, the pixel refers to the binned cell, not the detector element.

2.1. Atmospheric residuals

The residuals caused by atmospheric correction are large enough to obscure some absorption features, such as the water absorption around 1.4 μm. Also, they appear to be consistent not only in the along-track direction but also in the cross-track direction over several pixels. Fig. 1 shows representative examples. Fig. 1 (a) and (b) show some atmospherically corrected I/F spectra from the same column in the image "FRT00009312_07_IF166L_TRR3," compared with the transmission spectrum used for their correction by the volcano scan method. The transmission spectrum that minimizes artifacts is selected with an empirical optimization method implemented in the CAT software. Triplet-like spikes around 2.0 μm, a relatively small spike around 1.44 μm, and small dual spikes around 1.6 μm are likely to be residuals caused by atmospheric correction because they coincide with absorption features shown in the atmospheric transmission spectrum (green). Overall, the current atmospheric correction exhibits a similar fluctuation pattern in the 1.0-1.7 μm and 2.0 μm regions of the corrected spectra along the cross-track column. Furthermore, Fig. 1 (c) and (d) indicate that the similar pattern of fluctuations is also consistently observed across the cross-track direction over several pixels. This suggests that the systematic pattern is likely to be the

residual of atmospheric correction rather than a calibration error, under the assumption of the uniformity of atmospheric transmission.

These artifacts are not fully removed even in the most advanced TER products. Fig. 2 shows the same analysis on the corresponding TER I/F product, as performed in Fig. 1. One can still observe a similar fluctuation pattern on the spectra both along the column and across several neighboring columns, although the shape of such a pattern changes on the spectra in Fig. 1 due to additional processing made for the TER product.

Such artifacts are also observed in the simulation of the volcano scan correction using radiative transfer modeling (Wiseman et al., 2016). As discussed in Wiseman et al. (2016), some are related to the violation of the assumptions made in the empirical volcano scan method. The empirical method requires that the atmospheric transmission spectrum at the Olympus Mons be exponentially scaled to the one in the image to be corrected by a single exponential factor. Differences in atmospheric conditions, such as the amounts of dust and ice aerosols, the amount of water vapor, and temperature and pressure, from those at Olympus Mons break this assumption, causing the artifacts. This problem is partly addressed by the optimal selection of transmission spectrum from the several empirically derived transmission spectra measured in different seasons and different atmospheric conditions, although the small collection of the empirically derived spectra is unlikely to be sufficient to fully consider temporal and spatial variations. In addition, Wiseman et al. (2016) showed that the absorption coefficient of carbon dioxide for each wavelength channel is not constant along the optical path due to the vertical variation of the Martian atmosphere.

Furthermore, there is another limitation in the empirical volcano scan method – the violation of the log-linearity of the transmission spectrum empirically obtained from the CRISM instrument. The reason is that the Martian gaseous atmospheric transmission spectrum has many much narrower absorption bands than the spectral resolution of the CRISM instrument. Therefore, even if the Martian atmosphere was vertically uniform, the empirically obtained transmission spectrum could not be scaled to exactly cancel out the transmission component of the measured I/F spectrum. We refer the reader to Appendix B for a more rigorous explanation on this issue.

2.2. Random noise

There are several sources of random noise in CRISM images. The behavior of noise at each detector element over time can be observed within the profile in the along track direction because the along-track direction is equivalent to the "time" direction as CRISM is a pushbroom scanner. Fig. 3 shows representative examples of four different aspects of the along-track dynamics of the noise – an example of a "good" detector and three different kinds of "bad" detectors, together with a spectrum that intersects those profiles. The residual[1] profiles in the along-track direction of bad detectors are shown in black and that of a good detector is in red in Fig. 3 (b)-(d). Each of the bad detectors shows different time dependent behaviors: autoregressive random noise, random spikes, and a telegraph pattern. The residual profile shown in black in Fig. 3 (b) is always larger than zero and seems to be highly related to its previous residual, indicating a strong autoregressive property. The black profile in Fig. 3 (c) shows mostly small variance (but slightly larger than that of the good detector shown in red) and often corrupted with spiky noise of various magnitudes. The occurrence of spikes seems to be random. Finally, the black profile in Fig. 3 (d) shows a clear telegraph noise, exhibiting occasional sudden step-like transitions between two levels. These different sources of noise, which confirm and expand previous observations by Parente et al. (2010), make wholistic statistical modeling difficult. Fortunately when we observe a spectral profile, as shown in Fig. 3 (a), these various kinds of noise manifest themselves as spikes with varying magnitudes.

2.3. Interpolation bias

Some pixels are corrupted with elevated noise. In some pixels, only the value indicating saturation (4095 in the 12-bit format) is recorded in the raw image cube and therefore, no information relevant to radiative energy is measured. Those pixels are marked as "bad pixels" (BP), discarded, and replaced in the calibration by linear interpolation in the

[1]The residual of our atmospheric correction method, obtained by removing estimated atmospheric and surface components from I/F signal, is considered to be a suitable approximation of the noise in CRISM signals.

same wavelength channel of the spatial neighbors in the cross-track direction in each image frame (Murchie et al., 2007, 2016). If both sides of the neighboring pixels are not "bad", then linear interpolation is simply the mean of the neighbors.

The linear spatial interpolation of BPs sometimes causes small spikes, which we call *interpolation bias*. In a CRISM image, the continuum shapes of spatially neighboring spectra tend to be similar but their magnitudes do not completely align. In particular, the magnitude of the continuum of the spectrum does not correspond to the average of the continua of its two spatial neighbors. Every bad pixel (channel) that is replaced by the average of the spatial neighbors will exhibit a spike whose peak is exactly equal to that average. The overall effect of the interpolation is a "train" of spikes of similar magnitude. Fig. 4 shows three representative examples of the interpolation bias. The red spectrum has BPs marked with purple dots. These BPs are replaced with the interpolation of cross-track spatial neighbors, namely the mean (in yellow) of the two gray spectra, if the same bands of both of the neighbors are not marked as BPs themselves.

The interpolation bias can be alleviated by the filtering stage in the TRR3 processing pipeline. The comparison of atmospherically corrected I/F spectra with (blue) or without (red) filtering in Fig. 4 (a) shows that filtering largely removes isolated spikes over 1.6-2.6 μm. However, the filter is sensitive to the occurrence of many adjacent BPs. A spurious artifact is created around 1.37 μm where there is a concentration of BPs. Fig. 4 (b) shows spike clusters are left over after filtering. Fig. 4 (c) shows a spurious absorption created by the filter in a range affected by many adjacent BP's. This phenomenon also explains the emergence of *spike clusters* and *spurious absorptions* investigated by Leask et al. (2018).

The interpolation bias often occurs when the spectral continuum or shape changes rapidly in the spatial domain. In particular, it tends to happen in small areas that are spectrally distinctive from its surroundings. The BPs and interpolation bias occur more frequently on spatially binned images (HRL and HRS).

2.4. Water ice aerosols

Depending on seasons and locations, the Martian atmosphere may contain water ice aerosols, which may significantly affect acquired spectra (Wiseman et al., 2016). It is reported that a significant amount of water ice aerosols is observed at low latitudes near aphelion (Clancy, 2003), which corresponds to observation IDs A***, B***, C***, 18***, or 24***. Water ice aerosol spectra are characterized by significant absorptions at 1.5 and 2.0 μm, a shallow wide absorption over 2.3 μm, and a downward slope over 2.6 μm wavelength region toward longer wavelengths. The presence of water ice aerosols in CRISM I/F spectra could be visually confirmed by the observation of both an absorption at 1.5 μm that may look like a downward continuum shift and a depression around 2.0 μm (e.g., Fig. 5). The depression around 2.0 μm may not be sufficient by itself to confirm the presence of water ice aerosols because it could be a bowl-shape artifact (Morgan et al., 2011; Wiseman et al., 2016). The feature at 2.0 μm can mask a mineral hydration feature at 1.9 μm. While some atmospheric transmission spectra stored as "VS" in the ancillary data records (ADR) consider the presence of the water ice aerosol, the set is not extensive.

3. Method

Our proposed combined atmospheric correction and de-noising method aims to derive a refined atmospheric transmission spectrum from the observed I/F spectra within the image, while simultaneously detecting large noise. The computed transmission spectrum is then used for atmospheric correction. The surface contribution and the transmission spectrum and its scaling parameters are simultaneously determined through a minimization process. In order to avoid interpolation bias and subsequent artifacts, our method is performed on I/F spectra produced by our own implementation of the calibration pipeline (Murchie et al., 2016) without applying TRR3 filtering or interpolating BPs. First, we describe the signal model adopted in our method, including a spectral mixing model for the surface and a model for atmospheric transmission, and then discusses the adopted methodology to perform the estimation of the atmospheric transmission spectrum and atmospheric compensation.

3.1. Signal model

Let us denote the observed signal (I/F) at one pixel by $\boldsymbol{y} \in \mathbb{R}^{L\times 1}$ where L is the number of wavelength channels, its associated surface reflectance by $\boldsymbol{r} \in \mathbb{R}^{L\times 1}$, and its atmospheric transmission spectrum by $\boldsymbol{t} \in \mathbb{R}^{L\times 1}$. Assuming that the spectral contribution of the atmosphere is uniform along the optical path, the signal model under the Beer-Lambert law is:

$$y_i = t_i^{\beta} r_i, \tag{1}$$

for all $i = 1, \ldots, L$, where y_i, t_i, and r_i are the ith elements of $\boldsymbol{y}$, $\boldsymbol{t}$, and $\boldsymbol{r}$, respectively, and β is a scaling parameter that depends on the optical path length. Since I/F, transmission, and surface reflectance are all assumed to be positive, the observed signal $\boldsymbol{y}$ is readily converted to the logarithmic domain:

$$\log(y_i) = \beta \log(t_i) + \log(r_i) \tag{2}$$

for all $i = 1, \ldots, L$. In this domain, the transmission spectrum present in all pixels is interpreted as an additive component to the surface reflectance. For the sake of simplicity, let us express the element-wise logarithmic operation on a vector $\boldsymbol{x}$ (on a matrix $\mathbf{X}$) as $\mathbf{log}\,\boldsymbol{x}$ ($\mathbf{log}\,\mathbf{X}$). Then the vector form of equation (2) will be

$$\mathbf{log}\,\boldsymbol{y} = \beta\,\mathbf{log}\,\boldsymbol{t} + \mathbf{log}\,\boldsymbol{r}. \tag{3}$$

Let us collect the spectra in the same cross-track column and denote the lateral stacks of the observed I/F and the surface reflectance spectra by $\mathbf{Y} \in \mathbb{R}^{L\times N}$ and $\mathbf{R} \in \mathbb{R}^{L\times N}$ respectively, where N is the number of lines in the along-track direction. If we assume that the atmospheric transmission spectrum is constant in the along-track direction, we have

$$\mathbf{logY} = (\mathbf{log}\,\boldsymbol{t})\,\boldsymbol{\beta}^{\mathsf{T}} + \mathbf{logR}, \tag{4}$$

where $\boldsymbol{\beta} \in \mathbb{R}^{N\times 1}$ is the concatenation of the β coefficients for all measurements in the column. The whole image cube is not stacked together because measured atmospheric spectra are different depending on cross-track columns due to smile effects of the CRISM instrument.

Next, we introduce a model for the surface reflectance. We start with a well-known linear mixing model (LMM). LMM models a single measured spectrum as the linearly weighted sum of pure endmember spectra according to their fractional abundances. This assumption would be valid in a "checkerboard" configuration, where the footprint of the measured spectrum would encompass several surface areas each composed of a pure mineral endmember. Although this is not always a reasonable assumption, our goal is not to accurately model mineral abundances but rather to accurately model the shape of the surface spectrum to isolate the effect of the atmosphere. Recently, we extended the LMM to consider an adaptive background (LMM-AB) (LMM-AB) (Itoh and Parente, 2017b):

$$\mathbf{R} = \mathbf{AX} + \mathbf{B} \quad (\mathbf{X} \succeq \mathbf{0}), \tag{5}$$

where $\mathbf{A} \in \mathbb{R}^{L \times N_A}$ (N_A is the number of endmembers) is a spectral library matrix whose columns correspond to endmember spectra, $\mathbf{X} \in \mathbb{R}^{N_A \times N}$ is a matrix whose columns store abundances of endmembers for observed spectra, $\mathbf{B} \in \mathbb{R}^{L \times N}$ is a matrix whose columns represent concave background spectra, and $\succeq$ represents element-wise inequality. The concave background spectra are interpreted as continuum components, which are conventionally considered to be generally spectrally unremarkable (Clark and Roush, 1984; Clark, 1999; Clark et al., 2003). In addition, the concave background spectra fit the contribution of unknown dust aerosols prevalent on Mars that may give negative slopes in this wavelength region (Brown, 2014; Wiseman et al., 2016). Although the dust aerosols residing in the atmosphere cannot be considered as a part of surface, it improves the fit to the observed I/F spectra. We further modify the LMM-AB to a logarithmic LMM-AB:

$$\mathbf{logR} = (\mathbf{logA})\,\mathbf{X} + \mathbf{B} \quad (\mathbf{X} \succeq \mathbf{0}) \tag{6}$$

where $\mathbf{R}$ and $\mathbf{A}$ are replaced with their logarithmic versions and, in general, $\mathbf{X}$ and $\mathbf{B}$ in this model are not equivalent to those in equation (5). The conversion to the logarithm domain is mainly motivated by computational tractability in the formulation we present in the following section.

Combining the equations (4) and (6), the I/F signals can be modeled as

$$\log\mathbf{Y} = (\log \boldsymbol{t}) \cdot \boldsymbol{\beta}^{\mathsf{T}} + (\log\mathbf{A})\,\mathbf{X} + \mathbf{B}. \tag{7}$$

3.1.1. Library

We construct a "global" spectral library rather than a small spectral library for each image, aiming for wide applicability of our method with little customization. The spectral library $\mathbf{A}$ must be as large as possible to represent as many known endmembers so that it can accurately model all the possible mixed surface spectra encountered in the CRISM observations. This can be accomplished by using all the spectra of potential mineral phases in publicly available spectral databases, such as CRISM spectral library (Murchie et al., 2007), U.S. Geological Survey (USGS) spectral library (Clark et al., 2007), Reflectance Experiment Laboratory (RELAB) spectral database (NASA Reflectance Experiment Laboratory, 2014), and the Minerals Identified through CRISM Analysis (MICA) Library (Viviano-Beck et al., 2014). We select 686 spectra from the mineral group of the CRISM spectral library, splib06, and all the spectra from the MICA library.

The library endmember spectra are convolved with CRISM spectral channels using the ground calibrated band pass functions whose parameters are stored in the data labeled as "SB" in the CRISM calibration data records (CDR) (Murchie et al., 2007). The convolved endmember spectra are converted to logarithmic scale and normalized with respect to their ℓ_2-norm in the log-domain, where the ℓ_2-norm of a vector is the square root of the mean of the square of its elements. In our implementation, we further apply continuum removal to the normalized logarithmic endmember spectra. The continuum of each spectrum here is defined as the concave hull that minimally envelops it. Now the term $\mathbf{AX}$ represents the continuum-removed absorption features of the surface reflectance spectra. The removed continua are interpreted as a part of the background term since they are concave. The continuum removal increases the dissimilarity of the spectra in the library, also making computation faster. In addition, the continuum removal can be performed beforehand and cached for all WA files and therefore, the computational burden accompanied with this pre-processing is small. Although this continuum removal results in a different optimization

problem and it may have a different optimal solution, we confirmed that almost identical solutions are obtained while reducing computational time.

Our method operates in two modes depending on whether or not water ice aerosol contributions are taken into account. In the mode with water ice aerosols, the absorption efficiency of water ice is included into the library. Absorption efficiency of water ice aerosol is computed using miepython[2] based on a solution (Wiscombe, 1979) of Mie scattering theory. The input imaginary part of refractive index is obtained from the absorption coefficient data reported in Grundy and Schmitt (1998) with the relationship $k_a = 4\pi n_k/\lambda$ where k_a is the absorption coefficient, n_k is the imaginary part of the refractive index, and λ is the wavelength. The real part of it is obtained from the Grenoble Astrophysics and Planetology Solid Spectroscopy and Thermodynamics (GhoSST) database[3] that was originally reported by Warren (1984) and linearly interpolated to the wavelength samples of the absorption coefficients. Spherical shapes are assumed for the particles and in total, 27 absorption efficiency spectra with several different temperatures and nine different particle radii (0.5, 0.8, 1, 1.2, 1.5, 1.8, 2, 3, and 4 μm) are created. These spectra are convolved to CRISM wavelength channels as done on the mineral spectra using CDR SB data and added to the library $\mathbf{A}$.

3.2. Atmospheric correction and de-noising

Based on this model, we estimate the true transmission spectrum given the observation $\mathbf{Y}$ and the library matrix $\mathbf{A}$. It is reasonable to assume that the true $\mathbf{\log} \boldsymbol{t}$ could fit the model sufficiently well. A straightforward way to assess the quality of fit is a loss function defined by a norm of the error. In order to achieve robustness to various random noise sources described in Section 2.2, we opt for the ℓ_1-norm of the error, equivalent to the absolute sum of the errors (ASE):

$$L_{\mathrm{ASE}}(\mathbf{\log Y}, \mathbf{\log} \boldsymbol{t}, \boldsymbol{\beta}, \mathbf{X}, \mathbf{B}) = \left\| \mathbf{\log Y} - \mathbf{\log} \boldsymbol{t} \cdot \boldsymbol{\beta}^{\mathsf{T}} - (\mathbf{\log A})\, \mathbf{X} - \mathbf{B} \right\|_{1,1}, \tag{8}$$

where $\|\mathbf{M}\|_{1,1}$ represents the sum of absolute values of all the elements in $\mathbf{M}$. The ℓ_1-norm of a vector is the sum of absolute values of its elements and $\|\cdot\|_{1,1}$ is the equivalent operator

[2]https://github.com/scottprahl/miepython

[3]http://ghosst.obs.ujf-grenoble.fr

for matrices. Model inversion based on ℓ_1-errors is known to be robust to corruptions such as dense large random spikes, while the more commonly used ℓ_2-errors assume that the noise follows a Gaussian distribution and perform poorly in the presence of such noise (Wright et al., 2009; Wright and Ma, 2010).

It is reasonable to assume that the number of endmembers composing each mixed surface spectrum is small. Then, given a large global library matrix $\mathbf{A}$, our goal is to find a combination of a small number of endmembers, in other words, a sparse $\mathbf{X}$, the transmission spectrum, and its scaling parameter that fit the model well enough in terms of the ASE (8). Such a solution is approximately obtained by adding a ℓ_1-norm penalty on $\mathbf{X}$, known as a sparsity promoting regularizer, to the minimizing function (Iordache et al., 2011). We define a cost function:

$$f(\mathbf{log Y}, \mathbf{log}\, \boldsymbol{t}, \boldsymbol{\beta}, \mathbf{X}, \mathbf{B}) = L_{\mathrm{ASE}}(\mathbf{log Y}, \mathbf{log}\, \boldsymbol{t}, \boldsymbol{\beta}, \mathbf{X}, \mathbf{B}) \; + \; \|\boldsymbol{\Lambda} \odot \mathbf{X}\|_{1,1},$$

where $\boldsymbol{\Lambda}$ is a $N_A \times N$ matrix whose elements are trade-off parameters controlling the sparsity of $\mathbf{X}$ and $\odot$ represents element-wise multiplication. Consider the minimization problem:

$$\begin{aligned} \underset{\mathbf{log}\, \boldsymbol{t}, \boldsymbol{\beta}, \mathbf{X}, \mathbf{B}}{\text{minimize}} \quad & f(\mathbf{log Y}, \mathbf{log}\, \boldsymbol{t}, \boldsymbol{\beta}, \mathbf{X}, \mathbf{B}) \\ \text{subject to} \quad & \mathbf{X} \succeq \mathbf{0}, \mathbf{CB} \succeq \mathbf{0}, \end{aligned} \tag{9}$$

where $\mathbf{C}$ is a concavity preserving operator defined by:

$$C_{i,j} = \begin{cases} (w_{i+2} - w_i) & \text{if } i+1 = j \\ -(w_{i+2} - w_{i+1}) & \text{if } i = j \\ -(w_{i+1} - w_i) & \text{if } i = j+2 \\ 0 & \text{otherwise} \end{cases}, \tag{10}$$

where w_i is the center wavelength position of the ith wavelength channel. Each row of $\mathbf{CB} \succeq \mathbf{0}$ represents a window of three consecutive channels (the first row represents the window of the first three channels, the second does that from the second to fourth channels, and so on). Each of the inequalities ensures that the middle point of the three channels is above the line determined by the other two adjacent points, ensuring concavity of the

curvature over the three channels. The collection of these inequalities over all the windows constrains the whole curvature to be concave so that no absorptions are artificially introduced by our method.

We note that sparsity constrained unmixing on CRISM images has been proposed for the purpose of mineral mapping in the literature (Lin et al., 2016; Lin and Zhang, 2017; Lin et al., 2019). Our method is different because the main purpose is to perform atmospheric correction and de-noising. Furthermore, the formulation is novel in three aspects – 1) the effect of the atmosphere is integrated and the method is combined with atmospheric correction, 2) the logarithmic domain is considered, and 3) the ℓ_1-norm is considered as a loss function.

The function to be optimized in Eq. (9) is non-convex, making it difficult to find an optimal solution. We propose a variable splitting alternating optimization algorithm. The variables are separated into two groups, $(\boldsymbol{\beta}, \mathbf{X}, \mathbf{B})$, which represents continuum and surface contributions, and $(\mathbf{log}\, \boldsymbol{t})$, which represents the atmospheric transmission, so that the minimization with regard to each group becomes easier to handle. The algorithm alternates between three operations. First, surface and continuum parameters for all the spectra in the column are estimated using the current atmospheric transmission spectrum. Then channels of $\mathbf{logY}$ exhibiting unusually high values in the residual of the model (Eq. (8)) are flagged and replaced by the corresponding model estimate $(\mathbf{log}\, \boldsymbol{t}) \cdot \boldsymbol{\beta}^{\mathsf{T}} + (\mathbf{logA})\, \mathbf{X} + \mathbf{B}$, the right hand side of Eq. (7) substituted by the current estimated parameters. Finally, a single atmospheric spectrum is estimated from the surface and continuum spectra in the column. It is also important to properly initialize the atmospheric transmission spectrum for this non-convex optimization problem. We use the collection of the empirically derived transmission spectra in the ADR distributed with the CAT software. The detailed description of the algorithm to solve this minimization problem including the initialization of $\mathbf{log}\, \boldsymbol{t}$ is presented in Appendix A.

After the minimization problem is solved, atmospherically corrected log I/F, $\mathbf{logY}_{\mathrm{corr}}$ is

finally obtained by

$$\mathbf{log}\mathbf{Y}_{\mathrm{corr}} = \mathbf{log}\mathbf{Y} - (\mathbf{log}\,\boldsymbol{t}^{\star}) \cdot \boldsymbol{\beta}^{\star\mathsf{T}}, \tag{11}$$

where $\mathbf{log}\,\boldsymbol{t}^{\star}$ and $\boldsymbol{\beta}^{\star}$ are the optimal solutions of the minimization problem (9). One might be tempted to use the learned surface contribution, $\mathbf{A}\mathbf{X}^{\star} + \mathbf{B}^{\star}$ where $\mathbf{X}^{\star}$ and $\mathbf{B}^{\star}$ are the optimal solutions of the problem (9), as the best candidate outputs for the atmospheric compensation algorithm. Indeed, they are smoother because they are the linear combination of a smooth background and the endmember spectra in the library $\mathbf{A}$; however, they are likely to underestimate uncertainty present in the signal. Our method models the surface spectra with moderate accuracy to achieve the precise estimation of the transmission spectrum. Since the estimation of surface model inside our algorithm is performed independently for each spectrum, it is possible that some minor variations due to noise would be fit by the surface model, leading to the over- and mis- interpretation of spectral shapes. On the other hand, the transmission spectrum is less likely to experience such problems because it is collectively estimated by using all the spectra in the column. In other words, our estimate of the surface need only be accurate enough to contribute to the model of the transmission spectrum and we are not interested in accurate estimation of surface mineral abundances at this stage. The correction (Eq. (11)) retains small random noise fluctuations in the observation, representing the uncertainty in the signal. In addition, we do not recommend to directly interpret the estimated abundances $\mathbf{X}^{\star}$ since multiple sets of abundance values could model a spectral curve equally well enough in the presence of noise (Lapotre et al., 2017). The surface unmixing result would need careful validation but this effort is beyond the scope of this contribution.

In case of the method with water ice, water ice components are also removed from I/F:

$$\mathbf{log}\mathbf{Y}_{\mathrm{corr}} = \mathbf{log}\mathbf{Y} - (\mathbf{log}\,\boldsymbol{t}^{\star}) \cdot \boldsymbol{\beta}^{\star\mathsf{T}} - \mathbf{log}\mathbf{A}_{\mathsf{ice}}\mathbf{X}_{\mathsf{ice}}, \tag{12}$$

where $\mathbf{log}\mathbf{A}_{\mathsf{ice}}$ and $\mathbf{X}_{\mathsf{ice}}$ are the part of $\mathbf{log}\mathbf{A}$ and $\mathbf{X}$ that correspond to water ice absorption efficiencies, respectively.

3.3. Prior determination of $\mathbf{\Lambda}$

The elements of the parameter matrix $\mathbf{\Lambda}$ are fixed to be equal to $(0.01 \cdot \|\mathbf{log}\, \boldsymbol{y}\|_2)$ for all library endmembers, where $\|\cdot\|_2$ represents the ℓ_2-norm of a vector. We performed our method on several data sets and found that this value is typical for a large set of images. Considering that I/F values normally range between $[0, 1]$, larger trade-off parameters are assigned for darker I/F spectra because noise is enhanced in the logarithmic domain for low I/F values. In the mode with water ice aerosols, the entries of $\mathbf{\Lambda}$ associated with the spectra of water ice is set to 0. Our method is applied to the wavelength region over 1.0-2.6 μm (bands 3 to 244). Note that $\mathbf{\Lambda}$ is adjusted as iteration progresses (See Appendix A.5 for details).

3.4. Prior exclusion and post substitution of BPs

Some of the pixels in the image frames are severely corrupted by noise to an extent that would negatively affect the performance of our method. In our implementation, the significantly corrupted BPs detected at the early stage in the calibration are still excluded from all the image frames ahead of processing, although it is possible to apply our method without any prior exclusion of BPs. The BP information is extracted from CDR BP data derived from dark frame measurements prior (and post, if it exists) scene measurements. These BPs are substituted with the model estimate after our atmospheric correction and de-noising method is performed.

4. Results

We performed our proposed atmospheric correction and de-noising method on more than one hundred CRISM images in North East Syrtis Major, Jezero Crater, and Columbia Hills. In our environment (Intel Core i7 2.6GHz (quad core) CPU and 16GB RAM), the computational time taken for each image is about one and half hours in the mode without water ice aerosols and two hours when they are included. This excludes the time for library convolution. We present some representative examples of our method, comparing them with the outcome of the current CRISM processing pipeline: TER data products (when available)

or TRR3 I/F images atmospherically corrected by CAT. We validate our method with three approaches. The first is a visual check of the spectra to investigate whether or not artifacts are removed or distortions introduced. In the case of severe corruption due to elevated noise, we also compare our corrected spectra with atmospherically corrected non-filtered I/F. Such I/F data can be obtained by using I/F conversion implemented in CAT on TRR3 RA (radiance) data. We also perform inter-image comparison with the expectation that spectra of pixels from overlapping images at the same geographical locations should show similar spectral signatures if any overlapping images are available. All the atmospherically corrected spectra used for comparisons to our proposed results are processed with CAT 7.4 using the empirical selection of the transmission spectra and artifact correction. Photometric correction is not applied.

4.1. Removal of atmospheric residuals

Fig. 6 shows the comparison of I/F spectra corrected by CAT and those obtained by our proposed method. From Fig. 6 (a) and (c), our method significantly reduces the residuals over the 1.0-1.7 μm and 2.0 μm wavelength regions that are consistently observed for the spectra on the right. Furthermore, the 1.4 μm absorption feature is now clearly seen in the first and fourth spectra from the top on the left, while it is severely corrupted on their counterparts on the right. The appearance of that feature is plausible since it coincides with clear hydrated silica-like spectra that have bigger 1.9 μm hydration and 2.2 μm Al-OH bearing bands.

One may notice that the spectra in Fig. 6 (a) exhibit small high-frequency fluctuations that cannot be seen on the spectra in Fig. 6 (c). These are small zero-mean random noise components removed by TRR3 filtering for the input I/F of the CAT volcano scan, while not for the input I/F data to our method. Fig. 6 (b) shows that such small Gaussian-like noise is significantly reduced by spatial averaging, which confirms these fluctuations are not systematic artifacts. On the other hand, the systematic artifacts in the spectra in Fig. 6 (c) and (d) are not reduced with spatial averaging.

Our method also mitigates some consistent features in other wavelength regions such

as small spikes around 2.25, 2.30, 2.38, and 2.48 μm wavelengths. These spikes could be calibration errors or systematic errors caused by the empirical volcano scan method or minor variation in atmospheric conditions and the shift of the central wavelength of CRISM spectral channels, but their exact origins are hard to precisely identify.

Next we show some examples where a significant amount of water ice aerosols are observed. Fig. 7 shows the comparison of corrected I/F spectra by our method with water ice aerosols and those atmospherically corrected on TRR3 filtered I/F. The images of these spectra are measured at low latitudes near aphelion. For a variety of spectra, our method successfully mitigates the depression at 2.0 μm and the absorption at 1.5 μm caused by the water ice aerosol, together with other atmospheric residuals, and hydrated features at 1.4 and 1.9 μm are restored if they are present.

Our validation process follows several steps. The first step is direct comparison with CAT corrected filtered TRR3 or TER3 images. Fig 8 (a) shows such a comparison. The spectrum corrected by our method (in red) shows clearer absorption bands around 1.4, 1.9, and 2.0 μm wavelength regions than the CAT corrected spectrum in blue. Since our method substitutes model values to bad channels there is the potential of creating fictitious absorptions if too many adjacent channels are bad. By comparing the red spectrum with the corresponding spectrum without substitutions (in orange) we can confirm the shape of the band at 2.3 μm. Another validation method, illustrated in Fig. 8 (b), involves the spectra of a pixel at the same geographical location as the one in Fig. 8 (a) from an overlapping image. The spectrum corrected by our method displays the same absorption bands as the one in Fig 8 (a). Furthermore, a similarly shaped 1.9 μm absorption seems to be present in the spectrum in Fig. 8 (b), where the corrupted wavelength channels for the spectrum in Fig. 8 (a) are non noisy, confirming the shape of the water band in the spectrum of Fig. 8 (a).

The advantage of our substitution method is also shown in the spatial domain. Fig. 9 shows a comparison of band images corrected by our method and by CAT. The yellow rectangle highlights where such artifacts occur. In this highlighted area, sequential spatial columns are detected as BPs and are linearly interpolated with neighboring columns in the

CRISM calibration, which causes a smear. In contrast in Fig. 9 (b), this type of smear cannot be seen and finer spatial patterns become distinguishable.

4.2. Removal of noise and interpolation bias

In this section, we investigate the performance of our method in a scenario where detector noise is elevated and spectra are severely corrupted by interpolation bias. The first example in Fig. 10, shows a comparison of a spectrum corrected by our method (red) and two other spectra by volcano scan with (blue) and without (purple) TRR3 filtering. Overall, the spikes around 2.0 μm are greatly reduced in our corrected spectrum and the hydration band at 1.9 μm becomes clearer. The observation ID 2422E indicates that the image was taken near aphelion. The small absorption at 1.5 μm and a smooth depression around 2.0 μm on the blue spectrum indicate the existence of water ice aerosols, which seems to be removed in our corrected spectrum in addition to severe noise. Compared to the CAT-corrected filtered spectrum (blue), the red spectrum seems to add an absorption feature around 2.5 μm. The presence of this absorption is confirmed in the non-filtered spectrum (purple). When only the non-BP bands are plotted, an absorption around 2.5 μm can be observed. Since this wavelength region is contaminated by many spikes due to interpolation bias, we speculate that TRR3 filtering smoothed out the signal around 2.5 μm while creating a band around 2.6 μm.

Fig. 11 (a) and (b) show results of our method on the two spectra introduced in Fig. 4 (b) and (c). Our method is only minimally affected by interpolation bias (Fig. 11(a)) and does not show a spurious absorption around 2.1 μm that is observed in the CAT corrected spectrum (Fig. 11(b)). The non corrupted spectrum (in purple) in Fig. 11(b) shows a depression around the 2.0 μm wavelength region. We show that the depression is also an artifact by investigating multiple kinds of ratioed I/F in the same manner as the method described in (Leask et al., 2018). Under the assumption that the transmission spectrum is uniform along each column, the contribution of the atmospheric transmission could be removed by dividing a spectrum by another spectrally unremarkable in the same spatial column, whether or not they are atmospherically corrected. Fig. 11 (c) shows the ratios of

four versions of the spectrum in Fig. 11 (b), with color coding as explained in the caption. In all cases, we use as a denominator the geometric mean spectrum of the same spatial column, which, as we carefully verified, only contains atmospheric contributions. The big absorption feature at 2.1 μm observed in the filtered I/F (blue) with atmospheric correction is also in the one (light blue) without atmospheric correction, indicating the feature is unlikely to be an artifact created by the volcano scan correction. However, the feature can not be observed in the ratioed spectrum (green) of the non-filtered I/F without atmospheric correction. The many downward spikes on the green spectrum are due to interpolation bias. Therefore, the big absorption feature at 2.0 μm on the upper two spectra are likely to be an artifact created by TRR3 filtering due to dense BPs. This artifact corresponds to the *spurious feature* observed by (Leask et al., 2018). The ratioed spectrum (purple) of the non-filtered I/F with atmospheric correction shows an absorption around 2.0 μm, which is an artifact caused by an error in the estimation of the scaling parameter for the volcano scan correction.

Our method can also perform reasonable corrections in small outcrops. Fig. 12 (a)-(d) show a comparison of the atmospherically corrected spectra with the same three methods described in Fig. 10 of the same geographical location in four overlapping images. Our method consistently produces bland spectra while the CAT-corrected spectra shows a range of artifacts for different images. These spectra are affected by interpolation bias since this is a spatially small distinctive region as shown in Fig. 12 (e). The spectra corrected by the volcano scan using CAT exhibit anomalous shapes around the 2.0 μm wavelength region. The wide depression around 2.0 μm in the blue spectrum in Fig. 12 (a) and leftover spiky absorptions and a little depression around 2.0 μm in the blue spectra in Fig. 12 (b) and (c) is possibly a combination of the bowl-shape artifact and artifacts created by TRR3 filtering. A water ice like shape shown in the blue spectrum in Fig. 12 (c) is probably caused by uncorrected water ice aerosols. Indeed, the image with the observation ID 18781 from which the spectrum in Fig. 12 (c) is acquired near aphelion. We can validate our products in a way similar to the multiple ratio method we previously described.

More validation examples of our products are presented in the supplementary materials.

5. Potential limitations

Although our method is robust to noise and less affected by BPs, the occurrence of too many adjacent BPs in a spectrum could be problematic. Fig. 13 (a) shows an example of such a case. The red spectrum has been corrected by our method and the BPs have been substituted with the corresponding model values. The spectrum shows a 2.5 μm wavelength absorption, which is the shape suggested by the model. The orange spectrum, which has been corrected but with BP's that have been simply omitted, reveals that more than few sequential channels are bad. In such case, the shape of 2.5 μm cannot be easily corroborated. An image that contains a measurement of the same geographical location is shown in Fig 13 (b). The 2.5 μm wavelength region of that spectrum which does not require substitution shows no absorption features. The procedure lead us to reject the spectrum in Fig. 13 (a).

Fig. 14 shows another potential limitation, by which actual spectral features could be removed by our technique. In this figure, an absorption at 1.46 μm, a depression around 2.0 μm, and an absorption feature at 2.4 μm are removed by our method. While the 2.0 μm depression correction can be justified as a bowl-shape distortion, 1.46 μm and 2.4 μm are more problematic. However, those features are present everywhere along the column, which makes our method consider them as systematic column-dependent artifacts. While we cannot confirm that the features are atmospheric, the fact that they are present through the columns suggests that they are not due to surface contributions and therefore they can be corrected.

Another possible concern is the presence of an edge drop. The concave background might erroneously fit a downward large noise spike at the edge of a spectrum, which, therefore cannot be detected as a noise spike regardless of its magnitude. This problem can be seen in Fig. 7 (g). The spectra corrected by our method in these figures exhibit large drops around the right edge at 2.6 μm.

Additionally, since our method uses the transmission spectra in the ADR to initialize the image transmission spectrum, an image transmission spectrum that is dramatically different from those in the ADR library could also be an issue. The non-convex optimization may

not recover from a poor initialization. So far on all the images we have tested initialization using the ADR transmission appears to work well and no clear examples of the initialization leading to failure are seen.

Finally, our method could lead to erroneous results in scenes where water and carbon dioxide ice are present on the surface. In particular, in the presence of water ice aerosols, our method cannot discriminate ice aerosols from surface ice. The extension of the technique to such images will be the subject of a future publication.

6. Conclusion

In this paper, we proposed a new atmospheric correction and de-noising method for CRISM IR images of non-icy surfaces over the 1.0-2.6 μm wavelength range. Our method estimates the atmospheric transmission spectrum from the image itself by solving the minimization problem that unifies light propagation through the atmosphere and surface mixing, while large random noise spikes are simultaneously detected and removed. Experimental results show that our method significantly mitigates column-dependent systematic artifacts that could be caused by the volcano scan method using CAT, while successfully detecting and removing severe noise. Compared with CAT-correction, our correction provides a significant improvement over the 1.1-1.7 μm and 1.9-2.1 μm wavelength regions where the strong atmospheric absorptions of carbon dioxide are present. Our method has been applied to a large number of images of non-icy surfaces. The technique is also able to contend well with adverse conditions like elevated detector temperatures and water ice aerosols.

In addition, validations reveal that our method retrieves consistent spectral shapes for the same location in different overlapping images even in the presence of elevated noise. Another validation using ratioed spectra clarified that our method corrects for artifacts created in the calibration, such as interpolation bias.

We also advanced the understanding of noise and artifacts present in the CRISM IR images. We discovered the mechanism of the occurrence of *interpolation bias* formally reported by Leask et al. (2018). We also succeeded in extracting three different kinds of noise patterns present in CRISM scene images – an autoregressive pattern, random spikes and a telegraph

pattern. Finally, we presented a new theoretical limitation of the empirical volcano scan method.

Processed data are currently available upon request.

Acknowledgments

This work is supported by the NASA PDART NNX16AG48G. The authors acknowledge Arun Saranathan, Dr. Janice L. Bishop, Dr. Ralph Milliken, Rachel Sheppard, Jesse Tarnas, Dr. John Mustard, Dr. Frank P. Seelos, Dr. Raymond E. Arvidson, Dr. Scott Murchie, and the other members of the CRISM fandango team for providing valuable feedback for our spectral products.

Appendix A. An algorithm for optimization

In this appendix, we details the algorithm to solve the minimization problem (9). The minimization (9) is split into two easily solvable subproblems:

$$\begin{pmatrix} \boldsymbol{\beta}^{(k+1)} \\ \mathbf{X}^{(k+1)} \\ \mathbf{B}^{(k+1)} \end{pmatrix} = \underset{\substack{\boldsymbol{\beta},\mathbf{X},\mathbf{B} \\ \mathbf{X}\succeq\mathbf{0},\mathbf{CB}\succeq\mathbf{0}}}{\arg\min} \; f(\log \boldsymbol{t}^{(k)}, \boldsymbol{\beta}, \mathbf{X}, \mathbf{B}) \tag{A.1}$$

and

$$\log \boldsymbol{t}^{(k+1)} = \underset{\log \boldsymbol{t}}{\arg\min}\, f(\log \boldsymbol{t}, \boldsymbol{\beta}^{(k+1)}, \mathbf{X}^{(k+1)}, \mathbf{B}^{(k+1)}), \tag{A.2}$$

where k indicates an iteration number. De-noising is performed between those two operations in our algorithm.

The separation of the variable $\log \boldsymbol{t}$ from the other ones makes both of the problems solvable. Both of the subproblems (A.1) and (A.2) are convex optimization problems (Boyd and Vandenberghe, 2004) and have unique solutions, but their analytical solutions cannot be calculated. It is possible to use any solver (CVX (Grant and Boyd, 2008, 2014), CPLEX[4],

[4]https://www.ibm.com/analytics/cplex-optimizer

etc.) to solve them. In our implementation, we implemented a generalized version of alternating direction method of multipliers (ADMM) for fast convergence to moderate accuracy. In order to achieve the smaller computational time for the subproblems (A.1) and (A.2), the variables of the problems, including their dual variables, are initialized with their output variables in the last iteration (or the current values). Detailed algorithms for each problem are shown in the following sections below and supplement materials. Algorithm 1 summarizes a general methodology in the pseudo code format. The total number k_{maxiter} of iteration is currently fixed to 5.

Algorithm 1

Construct the concave preserving operator $\mathbf{C}$ using (10)
Initialize atmospheric transmission spectrum (See Appendix A.4)
for $k \leftarrow 1$ **to** k_{maxiter} **do**
    Solve the subproblem (A.1) (See Appendix A.1)
    Denoising (See Appendix A.3)
    Solve the subproblem (A.2) (See Appendix A.2)
    Update λ using (A.8) (See Appendix A.5)
    $k \leftarrow k + 1$
end for
Solve the subproblem (A.1) for final estimation

Appendix A.1. Subproblem (A.1)

The problem (A.1) is cast into a matrix form of constrained sparse least absolute deviation (CSLAD). Let us create a square matrix $\bar{\mathbf{C}} \in \mathbb{R}^{L \times L}$ by augmenting the first and last rows of $\mathbf{C}$ with cardinal vectors $\boldsymbol{e}_1 = [1, 0, \ldots, 0]^\mathsf{T} \in \mathbb{R}^L$ and $\boldsymbol{e}_L = [0, \ldots, 0, 1]^\mathsf{T} \in \mathbb{R}^L$, respectively:

$$\bar{\mathbf{C}} = [\, \boldsymbol{e}_1 \;\; \mathbf{C}^\mathsf{T} \;\; \boldsymbol{e}_L \,]^\mathsf{T}.$$

Since $\bar{\mathbf{C}}$ is a tri-diagonal matrix whose diagonal elements are nonzero, it is invertible. Let $\mathbf{Z} = \bar{\mathbf{C}}\mathbf{B}$, namely, we have $\boldsymbol{B} = \bar{\mathbf{C}}^{-1}\mathbf{Z}$. Let

$$\boldsymbol{\Gamma} = \begin{bmatrix} -\inf \cdot \mathbf{1}_{1\times N} \\ \mathbf{0}_{N-2\times N} \\ -\inf \cdot \mathbf{1}_{1\times N} \end{bmatrix},$$

where $\mathbf{1}_{1\times N}$ is a $1 \times N$ length vector with all the elements ones and $\mathbf{0}_{N-2\times N}$ is a $N-2 \times N$ matrix with all the elements zeros. The constraint $\mathbf{CB} \succeq \mathbf{0}$ is equivalently expressed as

$$\bar{\mathbf{C}}\mathbf{B} \succeq \boldsymbol{\Gamma} \Leftrightarrow \mathbf{Z} \succeq \boldsymbol{\Gamma}. \tag{A.3}$$

Therefore, the minimization problem (A.1) is equivalent to

$$\begin{aligned} \underset{\mathbf{X},\boldsymbol{\beta},\mathbf{Z}}{\text{minimize}} \quad & \left\|\mathbf{log}\mathbf{Y} - (\log \boldsymbol{t}^{(k)})\boldsymbol{\beta}^{\mathsf{T}} - (\mathbf{log}\mathbf{A})\mathbf{X} - \bar{\mathbf{C}}^{-1}\mathbf{Z}\right\|_{1,1} + \|\boldsymbol{\Lambda} \odot \mathbf{X}\|_{1,1} \\ \text{subject to} \quad & \mathbf{X} \succeq \mathbf{0} \text{ and } \mathbf{Z} \succeq \boldsymbol{\Gamma} \end{aligned}$$

Then the minimization problem is formalized into CSLAD:

$$\begin{aligned} \underset{\mathbf{S}}{\text{minimize}} \quad & \left\|\mathbf{log}\mathbf{Y} - \mathbf{G}^{(k)}\mathbf{S}\right\|_{1,1} + \|\hat{\boldsymbol{\Lambda}} \odot \mathbf{S}\|_{1,1} \\ \text{subject to} \quad & \mathbf{S} \succeq \hat{\boldsymbol{\Gamma}}, \end{aligned} \tag{A.4}$$

where

$$\mathbf{G}^{(k)} = [\, \log \boldsymbol{t}^{(k)} \;\; \mathbf{log}\mathbf{A} \;\; \bar{\mathbf{C}}^{-1} \,],$$

$$\mathbf{S} = \begin{bmatrix} \boldsymbol{\beta}^{\mathsf{T}} \\ \mathbf{X} \\ \mathbf{Z} \end{bmatrix}, \quad \hat{\boldsymbol{\Lambda}} = \begin{bmatrix} \mathbf{0}_{1\times N} \\ \boldsymbol{\Lambda} \\ \mathbf{0}_{L\times N} \end{bmatrix}, \quad \text{and} \quad \hat{\boldsymbol{\Gamma}} = \begin{bmatrix} \mathbf{0}_{1\times N} \\ \mathbf{0}_{N_A\times N} \\ \boldsymbol{\Gamma} \end{bmatrix}.$$

This optimization problem is readily solved via any convex optimization solvers such as CVX (Grant and Boyd, 2014, 2008) or CPLEX. Our implementation utilizes alternating direction method of multipliers (ADMM). We refer interesting readers to (Itoh and Parente, 2019b) for further details on our implementation.

Appendix A.2. Subproblem (A.2)

The subproblem (A.2) is cast as a matrix form of least absolute deviation (LAD) problem. The problem (A.2) is expressed as

$$\underset{\log \boldsymbol{t}}{\text{minimize}} \left\|\mathbf{log}\mathbf{Y} - (\log \boldsymbol{t})\boldsymbol{\beta}^{(k+1)^{\mathsf{T}}} - (\mathbf{log}\mathbf{A})\boldsymbol{X}^{(k+1)} - \mathbf{B}^{(k+1)}\right\|_{1,1}$$

Letting $\mathbf{R}_{\log \boldsymbol{t}}^{(k+1)} = \left(\mathbf{log Y} - (\mathbf{log A})\mathbf{X}^{(k+1)} - \mathbf{B}^{(k+1)}\right)$, the problem is interpreted as a matrix form of least absolute deviation:

$$\underset{\log \boldsymbol{t}}{\text{minimize}} \quad \left\|\mathbf{R}_{\log \boldsymbol{t}}^{(k+1)^{\mathsf{T}}} - \boldsymbol{\beta}(\log \boldsymbol{t})^{\mathsf{T}}\right\|_{1,1} \tag{A.5}$$

As with CSLAD, LAD can be solved via any convex optimization solvers. Again, we refer interesting readers to (Itoh and Parente, 2019b) for further details on our implementation.

Appendix A.3. De-noising step

Denoising is performed by a hard-thresholding on each element of the residual

$$\left|\mathbf{log Y} - \log \boldsymbol{t}^{(k)} \cdot \boldsymbol{\beta}^{(k+1)^{\mathsf{T}}} - (\mathbf{log A})\,\mathbf{X}^{(k+1)} - \mathbf{B}^{(k+1)}\right|$$

The thresholding value is empirically determined and fixed as 0.015 except for the initialization step as described in Appendix A.4. If an element of the residual is above the threshold value, then the corresponding element of $\mathbf{log Y}$ is replaced with its model value:

$$\log \boldsymbol{t}^{(k)} \cdot \boldsymbol{\beta}^{(k+1)^{\mathsf{T}}} + (\mathbf{log A})\,\mathbf{X}^{(k+1)} + \mathbf{B}^{(k+1)}.$$

Appendix A.4. Initialization

Next, we discuss approaches we used to obtain desirable solution by our algorithm. Since the minimization problem (9) is a non-convex optimization problem, it is heavily influenced by initialization. With the moderately accurate initialization of the transmission spectrum, especially its concave component, the background matrix $\mathbf{B}$ is unlikely to learn the concave component of the transmission spectrum. Therefore, it is crucial to initialize the transmission spectrum accurately enough. We initialize $\boldsymbol{t}$ with a linear combination of calibrated transmission spectra in the ADR data. To be precise, we solve the following minimization problem to initialize the transmission spectrum:

$$\begin{aligned} &\underset{\boldsymbol{\Phi},\mathbf{X},\mathbf{B}}{\text{minimize}} \quad \left\|\mathbf{log Y} - [\mathbf{log T}_{\mathrm{A}}\ \mathbf{log A}]\begin{bmatrix}\boldsymbol{\Phi}^{\mathsf{T}} \\ \mathbf{X}\end{bmatrix} - \mathbf{B}\right\|_{1,1} + \|\boldsymbol{\Lambda} \odot \mathbf{X}\|_{1,1} \\ &\text{subject to} \ \ \mathbf{X} \succeq \mathbf{0}, \mathbf{CB} \succeq \mathbf{0}, \boldsymbol{\Phi} \succeq \mathbf{0} \end{aligned} \tag{A.6}$$

where $\mathbf{T}_{\mathrm{A}} \in \mathbb{R}^{L \times N_T}$ (N_T is the number of ADR transmission spectra) is the concatenation of all the transmission spectra in the ADR. After the solution is obtained, de-noising is

performed using the absolute value of the residual, safeguarded with the standard deviation of the residual of each pixel. If the absolute value of the residual is greater than 0.1 and the standard deviation of the pixel is lower than 0.15, then the pixel is marked as a bad entry and replaced with its model estimate. The rationale for the safeguarding with the standard deviation is to retain pixels that show small random variation and huge constant bias due to calibration or processing errors. Then, $\mathbf{log}\,\boldsymbol{t}$ is initialized by solving

$$\underset{\mathbf{log}\,\boldsymbol{t}}{\text{minimize}} \left\| \mathbf{log}\mathbf{Y} - (\mathbf{log}\,\boldsymbol{t})\left(\boldsymbol{\Phi}^{\star}\mathbf{1}_{N_T}\right)^{\mathsf{T}} - (\mathbf{log}\mathbf{A})\mathbf{X}^{\star} - \mathbf{B}^{\star} \right\|_{1,1} \tag{A.7}$$

where $\mathbf{X}^{\star}$, $\mathbf{B}^{\star}$, and $\boldsymbol{\Phi}^{\star}$ are the optimizers of the minimization (A.6) and $\mathbf{1}_{N_T}$ is a $N_T \times 1$-length vector with all the elements equal to unity. Both of the problems (A.6) and (A.7) are convex optimizations and solved in ways similar to ones for (A.1) and (A.2) shown in Appendix A.1 and Appendix A.2, respectively.

We note that the transmission spectra of the ADR are compensated with their artifact factor stored in the same data before the initialization. The artifact spectra that correct the bowl-shape artifact around the 2.0 μm region are subtracted from the transmission spectra of the ADR. The artifact around the 2.0 μm wavelength region is too large and correlated with some endmember spectra of water ice or hydrated minerals, violating one of the assumptions of our method, which is a difficulty in modeling with CLMM. Integration of the artifact factor ahead of initialization prevents the large bowl-shape artifact, eliminating the violation.

Appendix A.5. Adjustment of the trade-off parameter

The selection and adjustment of $\boldsymbol{\Lambda}$ also affect the performance of our algorithm. $\boldsymbol{\Lambda}$ is the trade-off parameter that balances the weight on the sum of the squared residual and that on the sparsity of the dictionary matrix. It is important to keep the balance of the two terms at each iteration. We balance the cost of the two terms in accordance with an expected drop in the residual at a certain iteration. Our update scheme is

$$\boldsymbol{\Lambda} \leftarrow \boldsymbol{\Lambda} \cdot \frac{\left\| \mathbf{R}^{(k)}_{\text{new}} \right\|_{1,1}}{\left\| \mathbf{R}^{(k)}_{\text{old}} \right\|_{1,1}} \tag{A.8}$$

where

$$\mathbf{R}_{\text{old}}^{(k)} = \left| \mathbf{log Y} - \mathbf{log}\, \boldsymbol{t}^{(k-1)} \cdot \boldsymbol{\beta}^{(k)^{\mathsf{T}}} - (\mathbf{log A})\, \mathbf{X}^{(k)} - \mathbf{B}^{(k)} \right|$$
$$\mathbf{R}_{\text{new}}^{(k)} = \left| \mathbf{log Y} - \mathbf{log}\, \boldsymbol{t}^{(k)} \cdot \boldsymbol{\beta}^{(k)^{\mathsf{T}}} - (\mathbf{log A})\, \mathbf{X}^{(k)} - \mathbf{B}^{(k)} \right|.$$

Appendix B. A note on theoretical limitation of the empirical volcano scan method

This appendix describes a theoretical limitation of the empirical volcano scan method – the violation of the log-linearity of the transmission spectrum empirically obtained from the CRISM instrument:

$$\mathbf{log}\, \boldsymbol{y} = \beta\, \mathbf{log}\, \boldsymbol{t} + \mathbf{log}\, \boldsymbol{r}, \tag{B.1}$$

where $\boldsymbol{y} \in \mathbb{R}^L$ is an observed I/F spectrum vector, $\boldsymbol{r} \in \mathbb{R}^L$ is a surface reflectance spectrum vector, $\boldsymbol{t} \in \mathbb{R}^L$ is a transmission spectrum vector, β is a scalar representing path length, and the operator $\mathbf{log}\,\cdot$ represents the element-wise logarithmic operation of a vector. The violation of the log-linearity of the transmission was also discussed in (Wiseman et al., 2016) under the simulated Martian atmospheric condition. We will show that the violation may occur even under much simpler conditions – the Beer-Lambert model with constant pressure and temperature without scattering. The decomposition (B.1) is the basic principle that supports the empirical volcano scan method. At a first look, the principle seems to be justified by assuming the uniformity of the atmospheric transmission spectrum and the Beer-Lambert law for radiative propagation. Even under this ideal condition, the principle itself does not hold for the implementation using the CRISM measurements because of its insufficient wavelength resolution. We will clarify this in the following paragraphs.

The actual sensing process is expressed by the convolution of a continuous I/F spectrum with a spectral bandpass function. The spectral bandpass function models how each detector element reacts to an input radiation spectrum. An ideal spectrometer could perfectly split the light into wavelength components and its spectral response function would be a rectangle centered at the designed center wavelength of the channel. Practically such perfect

spectroscope is unattainable and a spectral bandpass function is modeled as a function that peaks at the designed center wavelength of the channel, drops toward both of the wings, and converging to zero. The measured I/F at the ith wavelength channel, namely the ith element of $\boldsymbol{y}$, is modeled as

$$y_i = \int_{\mathcal{C}_i} r(w) e^{-\beta k(w)} f_i(w) dw, \tag{B.2}$$

where y_i is the ith element of the measured I/F spectrum vector $\boldsymbol{y}$, $r(w)$ and $k(w)$ are a continuous reflectance spectrum and a continuous absorption coefficient spectrum as a function of wavelength w, respectively, $f_i(w)$ is the spectral bandpass function of the ith channel ($i = 1, \ldots, L$) satisfying $\int f_i(x)dx = 1$, and $\mathcal{C}_i$ is the effective range of $f_i(w)$ outside of which the function sufficiently rolls off to zero and is thus negligible, namely $\int_{\mathcal{C}_i} f_i(x)dx \approx 1$. Note that the absorption coefficient k is the logarithm of the transmission, namely, $k = \log t$. In case of CRISM imager, the band pass function is modeled as the summation of three Gaussian functions (Murchie et al., 2007).

The right hand side of (B.2) is, in general, not log-linear with respect to β. The decoupling shown in (B.1) requires an additional assumption: $r(w)$ and $k(w)$ are approximately constant over the effective range. If this assumption should be true, $r(w)$ and $k(w)$ would be reasonably taken out of the integration, making decoupling possible:

$$y_i \approx \bar{r}_i e^{-\beta \bar{k}_i} \int_{\mathcal{C}_i} f_i(w) dw \approx \bar{r}_i e^{-\beta \bar{k}_i} \cdot 1$$

where $\bar{r}_i$ and $\bar{k}_i$ are the approximated mean values of $r(w)$ and $k(w)$ over the range $\mathcal{C}_i$, respectively. Then, the transmission spectrum is empirically estimated by

$$t_i^{\mathrm{emp}} = \frac{\int_{\mathcal{C}_i} e^{-\beta_{\mathrm{btm}} k(w)} f_i(w) dw}{\int_{\mathcal{C}_i} e^{-\beta_{\mathrm{top}} k(w)} f_i(w) dw} \approx e^{-(\beta_{\mathrm{btm}} - \beta_{\mathrm{top}})\bar{k}_i}, \tag{B.3}$$

for $i = 1, \ldots, L$, where β_{btm} and β_{top} are the path lengths associated with the CRISM measurements at the bottom and top of Olympus Mons, respectively. Finally, the transmission spectrum for each pixel the scene is simply obtained by scaling with a single scaling parameter α: $t_i = (t_i^{\mathrm{emp}})^{\alpha}$ ($i = 1, \ldots, L$).

The assumption that $r(\lambda)$ and $k(\lambda)$ are approximately constant over $\mathcal{C}_i$ indicates that their variation is sufficiently broader than the width of the effective range. Put another way, the width of the effective range, which is roughly represented by the full-width-half-maximum (FWHM) of the spectral response function, needs to be sufficiently smaller than the scale of the variation of $r(\lambda)$ and $k(\lambda)$. While this may be valid for the surface reflectance, this assumption is hardly true for the absorption coefficient spectrum of the atmosphere. The absorption coefficient spectrum of CO_2, which could be simulated using the absorption line parameters in the HITRAN database (Gordon et al., 2017), exhibits many much narrower bands than the full-width-half-maximums of the CRISM wavelength channels. Thus, the empirically derived transmission spectrum vector t_i^{emp} cannot be scaled to the transmission spectrum vector with arbitrary path length. It will cause a static error when the path length β is same over pixels.

The bowl-shape artifact around the $2\,\mu$m wavelength region might be explained by this static error. Many isotopes of gaseous carbon dioxide have many narrow strong absorption bands around this region. The absorption coefficient spectrum varies a lot within one wavelength channel of CRISM. The approximated transmission spectrum (B.3) is not guaranteed to accurately model the transmission spectrum with arbitrary path length. The similar pattern of the residual seen over the 1.0-2.0 μm region could be also explained by this error. Further investigation is necessary on this aspect.

References

Arvidson, R.E., Squyres, S.W., Bell, J.F., Catalano, J.G., Clark, B.C., Crumpler, L.S., De Souza, P.A., Fairén, A.G., Farrand, W.H., Fox, V.K., Gellert, R., Ghosh, A., Golombek, M.P., Grotzinger, J.P., Guinness, E.A., Herkenhoff, K.E., Jolliff, B.L., Knoll, A.H., Li, R., McLennan, S.M., Ming, D.W., Mittlefehldt, D.W., Moore, J.M., Morris, R.V., Murchie, S.L., Parker, T.J., Paulsen, G., Rice, J.W., Ruff, S.W., Smith, M.D., Wolff, M.J., 2014. Ancient aqueous environments at endeavour crater, mars. Science (80-.). 343, 1–9. doi:10.1126/science.1248097.

Bibring, J.P., Langevin, Y., Mustard, J.F., Poulet, F., Arvidson, R., Gendrin, A., Gondet, B., Mangold, N., Pinet, P., Forget, F., Berthe, M., Bibring, J.P., Gendrin, A., Gomez, C., Gondet, B., Jouglet, D., Poulet, F., Soufflot, A., Vincendon, M., Combes, M., Drossart, P., Encrenaz, T., Fouchet, T., Merchiorri, R.,

Belluci, G., Altieri, F., Formisano, V., Capaccioni, F., Cerroni, P., Coradini, A., Fonti, S., Korablev, O., Kottsov, V., Ignatiev, N., Moroz, V., Titov, D., Zasova, L., Loiseau, D., Mangold, N., Pinet, P., Doute, S., Schmitt, B., Sotin, C., Hauber, E., Hoffmann, H., Jaumann, R., Keller, U., Arvidson, R., Mustard, J.F., Duxbury, T., Forget, F., Neukum, G., 2006. Global mineralogical and aqueous Mars history derived from OMEGA/Mars Express data. Science (80-.). 312, 400–404. doi:10.1126/science.1122659.

Boyd, S., Vandenberghe, L., 2004. Convex Optimization. Cambridge University Press.

Brown, A.J., 2014. Spectral bluing induced by small particles under the Mie and Rayleigh regimes. Icarus 239, 85–95. doi:10.1016/j.icarus.2014.05.042.

Brown, A.J., Hook, S.J., Baldridge, A.M., Crowley, J.K., Bridges, N.T., Thomson, B.J., Marion, G.M., de Souza Filho, C.R., Bishop, J.L., 2010. Hydrothermal formation of Clay-Carbonate alteration assemblages in the Nili Fossae region of Mars. Earth Planet. Sci. Lett. 297, 174–182. doi:10.1016/j.epsl.2010.06.018, arXiv:1402.1150.

Brown, A.J., Viviano, C.E., Goudge, T.A., 2020. Olivine-Carbonate mineralogy of the Jezero crater region. J. Geophys. Res. Planets 125. doi:10.1029/2019JE006011.

Bultel, B., Quantin, C., Lozach, L., 2015. Description of CoTCAT (complement to CRISM Analysis Toolkit). IEEE J. Sel. Top. Appl. Earth Obs. Remote Sens. 8, 3039–3049. doi:10.1109/JSTARS.2015.2405095.

Carter, J., Poulet, F., Murchie, S., Bibring, J.P., 2013. Automated processing of planetary hyperspectral datasets for the extraction of weak mineral signatures and applications to CRISM observations of hydrated silicates on Mars. Planet. Space Sci. 76, 53–67. doi:10.1016/j.pss.2012.11.007.

Carter, J., Viviano-Beck, C., Loizeau, D., Bishop, J., Le Deit, L., 2015. Orbital detection and implications of akaganéite on Mars. Icarus 253, 296–310. doi:10.1016/j.icarus.2015.01.020.

Clancy, R.T., 2003. Mars aerosol studies with the MGS TES emission phase function observations: Optical depths, particle sizes, and ice cloud types versus latitude and solar longitude. J. Geophys. Res. 108. doi:10.1029/2003JE002058.

Clark, R.N., 1999. Spectroscopy of rocks and minerals, and principles of spectroscopy, in: Rencz, A.N. (Ed.), Remote Sens. Earth Sci. Man. Remote Sens.. 3 ed.. John Wiley and Sons, Inc, New York. chapter 1, pp. 3–58.

Clark, R.N., Roush, T.L., 1984. Reflectance spectroscopy: Quantitative analysis techniques for remote sensing applications. J. Geophys. Res. Solid Earth 89, 6329–6340. doi:10.1029/JB089iB07p06329.

Clark, R.N., Swayze, G.A., Livo, K.E., Kokaly, R.F., Sutley, S.J., Dalton, J.B., McDougal, R.R., Gent, C.A., 2003. Imaging spectroscopy: Earth and planetary remote sensing with the USGS Tetracorder and expert systems. J. Geophys. Res. Planets 108, 5131. doi:10.1029/2002JE001847.

Clark, R.N., Swayze, G.A., Wise, R.A., Livo, K.E., Hoefen, T.M., Kokaly, R.F., Sutley, S.J., 2007. USGS Digital Spectral Library splib06a. Technical Report. Reston, VA. URL: http://pubs.er.usgs.gov/

publication/ds231.

Dundar, M., Ehlmann, B.L., Leask, E.K., 2019. Machine-learning-driven new geologic discoveries at Mars rover landing sites: Jezero and NE Syrtis arXiv:1909.02387.

Ehlmann, B.L., Edwards, C.S., 2014. Mineralogy of the Martian Surface. Annu. Rev. Earth Planet. Sci. 42, 291–315. doi:10.1146/annurev-earth-060313-055024.

Ehlmann, B.L., Mustard, J.F., Fassett, C.I., Schon, S.C., Head, J.W., Des Marais, D.J., Grant, J.A., Murchie, S.L., 2008a. Clay minerals in delta deposits and organic preservation potential on Mars. Nat. Geosci. 1, 355–358. doi:10.1038/ngeo207.

Ehlmann, B.L., Mustard, J.F., Murchie, S.L., Poulet, F., Bishop, J.L., Brown, A.J., Calvin, W.M., Clark, R.N., Des Marais, D.J., Milliken, R.E., Roach, L.H., Roush, T.L., Swayze, G.A., Wray, J.J., 2008b. Orbital identification of carbonate-bearing rocks on Mars. Science (80-.). 322, 1828–1832. doi:10.1126/science.1164759.

Ehlmann, B.L., Mustard, J.F., Swayze, G.A., Clark, R.N., Bishop, J.L., Poulet, F., Des Marais, D.J., Roach, L.H., Milliken, R.E., Wray, J.J., Barnouin-Jha, O., Murchie, S.L., 2009. Identification of hydrated silicate minerals on Mars using MRO-CRISM: Geologic context near Nili Fossae and implications for aqueous alteration. J. Geophys. Res. E Planets 114, 1–33. doi:10.1029/2009JE003339.

Gordon, I.E., Rothman, L.S., Hill, C., Kochanov, R.V., Tan, Y., Bernath, P.F., Birk, M., Boudon, V., Campargue, A., Chance, K.V., Drouin, B.J., Flaud, J.M., Gamache, R.R., Hodges, J.T., Jacquemart, D., Perevalov, V.I., Perrin, A., Shine, K.P., Smith, M.A.H., Tennyson, J., Toon, G.C., Tran, H., Tyuterev, V.G., Barbe, A., Császár, A.G., Devi, V.M., Furtenbacher, T., Harrison, J.J., Hartmann, J.M., Jolly, A., Johnson, T.J., Karman, T., Kleiner, I., Kyuberis, A.A., Loos, J., Lyulin, O.M., Massie, S.T., Mikhailenko, S.N., Moazzen-Ahmadi, N., Müller, H.S.P., Naumenko, O.V., Nikitin, A.V., Polyansky, O.L., Rey, M., Rotger, M., Sharpe, S.W., Sung, K., Starikova, E., Tashkun, S.A., Auwera, J.V., Wagner, G., Wilzewski, J., Wcisło, P., Yu, S., Zak, E.J., 2017. The HITRAN2016 molecular spectroscopic database. J. Quant. Spectrosc. Radiat. Transf. 203, 3–69. doi:10.1016/j.jqsrt.2017.06.038.

Goudge, T.A., Milliken, R.E., Head, J.W., Mustard, J.F., Fassett, C.I., 2017. Sedimentological evidence for a deltaic origin of the western fan deposit in Jezero crater, Mars and implications for future exploration. Earth Planet. Sci. Lett. 458, 357–365. doi:10.1016/j.epsl.2016.10.056.

Goudge, T.A., Mustard, J.F., Head, J.W., Fassett, C.I., Wiseman, S.M., 2015. Assessing the minearlogy of the watershed and fan deposits of the Jezero crater paleolake system, Mars. J. Geophys. Res. Planets 120, 775–808. doi:10.1002/2014JE004782.

Grant, M., Boyd, S., 2008. Graph implementations for nonsmooth convex programs, in: Blondel, V., Boyd, S., Kimura, H. (Eds.), Recent Adv. Learn. Control. Springer-Verlag Limited. Lecture Notes in Control and Information Sciences, pp. 95–110.

Grant, M., Boyd, S., 2014. CVX: Matlab software for fisciplined convex programming, version 2.1. http://cvxr.com/cvx.

Grundy, W.M., Schmitt, B., 1998. The temperature-dependent near-infrared absorption spectrum of hexagonal H_2O ice. J. Geophys. Res. Planets 103, 25809–25822. doi:10.1029/98JE00738.

He, L., O'Sullivan, J.A., Politte, D.V., Powell, K.E., Arvidson, R.E., 2019. Quantitative reconstruction and denoising method HyBER for hyperspectral image data and its application to CRISM. IEEE J. Sel. Top. Appl. Earth Obs. Remote Sens. PP, 1–12. doi:10.1109/JSTARS.2019.2900644.

Horgan, B.H., Anderson, R.B., Dromart, G., Amador, E.S., Rice, M.S., 2020. The mineral diversity of Jezero crater: Evidence for possible lacustrine carbonates on Mars. Icarus 339, 113526. doi:10.1016/j.icarus.2019.113526.

Iordache, M.D., Bioucas-Dias, J.M., Plaza, A., 2011. Sparse unmixing of hyperspectral data. IEEE Trans. Geosci. Remote Sens. 49, 2014–2039. doi:10.1109/TGRS.2010.2098413.

Itoh, Y., Parente, M., 2017a. Image-derived atmospheric transmission for enhancement of CRISM volcano scan correction, in: Lunar Planet. Sci. Conf. XLVIII, The Woodlands, TX. Abstract no. 2939.

Itoh, Y., Parente, M., 2017b. Sparse unmixing with adaptive background. IEEE Int. Geosci. Remote Sens. Symp. , 2593–2596.

Itoh, Y., Parente, M., 2018. A new scene dependent atmospheric transmission for enhancement of CRISM volcano scan correction, in: 49th Lunar Planet. Sci. Conf., The Woodlands, TX. Abstract no. 2337.

Itoh, Y., Parente, M., 2019a. A new simultaneous atmospheric correction and de-noising of CRISM data, in: 50th Lunar Planet. Sci. Conf., The Woodlands, TX. Abstract no. 2025.

Itoh, Y., Parente, M., 2019b. A note on alternating direction method of multipliers with generalized augmented terms for constrained sparse least absolute deviation. arXiv:1909.08558.

Kreisch, C.D., O'Sullivan, J.A., Arvidson, R.E., Politte, D.V., He, L., Stein, N.T., Finkel, J., Guinness, E.A., Wolff, M.J., Lapôtre, M.G., 2017. Regularization of Mars Reconnaissance Orbiter CRISM along-track oversampled hyperspectral imaging observations of Mars. Icarus 282, 136–151. doi:10.1016/j.icarus.2016.09.033.

Langevin, Y., Poulet, F., Bibring, J.P., Gondet, B., 2005. Sulfates in the north polar region of Mars detected by OMEGA/Mars Express. Science (80-.). 307, 1584–1586. doi:10.1126/science.1109091.

Lapotre, M.G., Ehlmann, B.L., Minson, S.E., 2017. A probabilistic approach to remote compositional analysis of planetary surfaces. J. Geophys. Res. Planets 122, 983–1009. doi:10.1002/2016JE005248.

Leask, E.K., Ehlmann, B.L., Dundar, M.M., Murchie, S.L., Seelos, F.P., 2018. Challenges in the search for perchlorate and other hydrated minerals With 2.1-μm absorptions on Mars. Geophys. Res. Lett. 45, 12180–12189. doi:10.1029/2018GL080077.

Lin, H., Mustard, J.F., Zhang, X., 2019. A methodology for quantitative analysis of hydrated minerals on

Mars with large endmember library using CRISM near-infrared data. Planet. Space Sci. 165, 124–136. doi:10.1016/j.pss.2018.11.005.

Lin, H., Zhang, X., 2017. Retrieving the hydrous minerals on Mars by sparse unmixing and the Hapke model using MRO/CRISM data. Icarus 288, 160–171. doi:10.1016/j.icarus.2017.01.019.

Lin, H., Zhang, X., Shuai, T., Zhang, L., Sun, Y., 2016. Abundance retrieval of hydrous minerals around the Mars Science Laboratory landing site in Gale crater, Mars. Planet. Space Sci. 121, 76–82. doi:10.1016/j.pss.2015.12.007.

McGuire, P.C., Bishop, J.L., Brown, A.J., Fraeman, A.A., Marzo, G.A., Frank Morgan, M., Murchie, S.L., Mustard, J.F., Parente, M., Pelkey, S.M., Roush, T.L., Seelos, F.P., Smith, M.D., Wendt, L., Wolff, M.J., 2009. An improvement to the volcano-scan algorithm for atmospheric correction of CRISM and OMEGA spectral data. Planet. Space Sci. 57, 809–815. doi:10.1016/j.pss.2009.03.007.

McGuire, P.C., Wolff, M.J., Smith, M.D., Arvidson, R.E., Murchie, S.L., Clancy, R.T., Roush, T.L., Cull, S.C., Lichtenberg, K.A., Wiseman, S.M., Green, R.O., Martin, T.Z., Milliken, R.E., Cavender, P.J., Humm, D.C., Seelos, F.P., Seelos, K.D., Taylor, H.W., Ehlmann, B.L., Mustard, J.F., Pelkey, S.M., Titus, T.N., Hash, C.D., Malaret, E.R., 2008. MRO/CRISM retrieval of surface Lambert Albedos for multispectral mapping of mars with disort-based radiative transfer modeling: Phase 1 – Using historical climatology for temperatures, aerosol optical depths, and atmospheric pressures. IEEE Trans. Geosci. Remote Sens. 46, 4020–4040. doi:10.1109/TGRS.2008.2000631, arXiv:0903.3687.

Milliken, R.E., Swayze, G.A., Arvidson, R.E., Bishop, J.L., Clark, R.N., Ehlmann, B.L., Green, R.O., Grotzinger, J.P., Morris, R.V., Murchie, S.L., Mustard, J.F., Weitz, C., 2008. Opaline silica in young deposits on Mars. Geology 36, 847–850. doi:10.1130/G24967A.1.

Morgan, F., Mustard, J.F., Wiseman, S.M., Seelos, F.P., Murchie, S.L., Mcquire, P.C., Team, T.C., 2011. Improved algorithm for CRISM volcano scan atmospheric correction, in: 42nd Lunar Planet. Sci. Conf., The Woodlands, TX. Abstract no. 2453.

Murchie, S., Arvidson, R., Bedini, P., Beisser, K., Bibring, J.P., Bishop, J., Boldt, J., Cavender, P., Choo, T., Clancy, R.T., Darlington, E.H., Des Marais, D., Espiritu, R., Fort, D., Green, R., Guinness, E., Hayes, J., Hash, C., Heffernan, K., Hemmler, J., Heyler, G., Humm, D., Hutcheson, J., Izenberg, N., Lee, R., Lees, J., Lohr, D., Malaret, E., Martin, T., McGovern, J.A., McGuire, P., Morris, R., Mustard, J., Pelkey, S., Rhodes, E., Robinson, M., Roush, T., Schaefer, E., Seagrave, G., Seelos, F., Silverglate, P., Slavney, S., Smith, M., Shyong, W.J., Strohbehn, K., Taylor, H., Thompson, P., Tossman, B., Wirzburger, M., Wolff, M., 2007. Compact Reconnaissance Imaging Spectrometer for Mars (CRISM) on Mars Reconnaissance Orbiter (MRO). J. Geophys. Res. E Planets 112, 1–57. doi:10.1029/2006JE002682.

Murchie, S., Guinness, E., Slavney, S., 2016. CRISM data software interface specification version 1.3.7.4.

Murchie, S.L., Mustard, J.F., Ehlmann, B.L., Milliken, R.E., Bishop, J.L., McKeown, N.K., Noe Dobrea,

E.Z., Seelos, F.P., Buczkowski, D.L., Wiseman, S.M., Arvidson, R.E., Wray, J.J., Swayze, G., Clark, R.N., Des Marais, D.J., McEwen, A.S., Bibring, J.P., 2009a. A synthesis of Martian aqueous mineralogy after 1 Mars year of observations from the Mars Reconnaissance Orbiter. J. Geophys. Res. E Planets 114, 1–30. doi:10.1029/2009JE003342.

Murchie, S.L., Seelos, F.P., Hash, C.D., Humm, D.C., Malaret, E., McGovern, J.A., Choo, T.H., Seelos, K.D., Buczkowski, D.L., Morgan, M.F., Barnouin-Jha, O.S., Nair, H., Taylor, H.W., Patterson, G.W., Harvel, C.A., Mustard, J.F., Arvidson, R.E., McGuire, P., Smith, M.D., Wolff, M.J., Titus, T.N., Bibring, J.P., Poulet, F., 2009b. Compact Reconnaissance Imaging Spectrometer for Mars investigation and data set from the Mars Reconnaissance Orbiter's primary science phase. J. Geophys. Res. E Planets 114, 1–15. doi:10.1029/2009JE003344.

Mustard, J.F., Murchie, S.L., Pelkey, S.M., Ehlmann, B.L., Milliken, R.E., Grant, J.A., Bibring, J.P., Poulet, F., Bishop, J., Dobrea, E.N., Roach, L., Seelos, F., Arvidson, R.E., Wiseman, S., Green, R., Hash, C., Humm, D., Malaret, E., McGovern, J.A., Seelos, K., Clancy, T., Clark, R., Marais, D.D., Izenberg, N., Knudson, A., Langevin, Y., Martin, T., McGuire, P., Morris, R., Robinson, M., Roush, T., Smith, M., Swayze, G., Taylor, H., Titus, T., Wolff, M., 2008. Hydrated silicate minerals on Mars observed by the Mars Reconnaissance Orbiter CRISM instrument. Nature 454, 305–309. doi:10.1038/nature07097.

Mustard, J.F., Poulet, F., Gendrin, A., Bibring, J.P., Langevin, Y., Gondet, B., Mangold, N., Bellucci, G., Altieri, F., 2005. Olivine and pyroxene diversity in the crust of Mars. Science (80-.). 307, 1594–1597. doi:10.1126/science.1109098.

NASA Reflectance Experiment Laboratory, 2014. Relab spectral database. available at http://www.planetary.brown.edu/relabdocs/relab.htm.

Ojha, L., Wilhelm, M.B., Murchie, S.L., Mcewen, A.S., Wray, J.J., Hanley, J., Massé, M., Chojnacki, M., 2015. Spectral evidence for hydrated salts in recurring slope lineae on Mars. Nat. Geosci. 8, 829–832. doi:10.1038/ngeo2546.

Parente, M., 2008. A new approach to denoising CRISM Images, in: Lunar Planet. Sci. XXXIX, The Woodlands, TX. p. 2528. doi:10.1029/2004JE002261.

Parente, M., Arvidson, R.E., Itoh, Y., Lin, H., Mustard, J.F., Saranathan, A.M., Seelos, F.P., Tarnas, J.D., 2019. Mineral detections over Jezero crater using advanced data processing techniques for CRISM data – The CRISM "Fandango", in: 9th Int. Conf. Mars, Pasadena, CA. Abstract no. 6382.

Parente, M., Clark, J.T., Brown, A.J., Bishop, J.L., 2010. End-to-end simulation and analytical model of remote-sensing systems: Application to CRISM. IEEE Trans. Geosci. Remote Sens. 48, 3877–3888. doi:10.1109/TGRS.2010.2050000.

Parente, M., Saranathan, A.M., Wiseman, S.M., Ehlmann, B., Pan, L., 2014. Denoising CRISM images: A new look, in: 45th Lunar Planet. Sci. Conf., The Woodlands, TX. p. 2900.

Poulet, F., Bibring, J.P., Mustard, J.F., Gendrin, A., Mangold, N., Langevin, Y., Arvidson, R.E., Gondet, B., Gomez, C., Berthe, M., Erard, S., Forni, O., Manaud, N., Poulleau, G., Soufflot, A., Combes, M., Drossart, P., Encrenaz, T., Fouchet, T., Melchiorri, R., Bellucci, G., Altieri, F., Formisano, V., Fonti, S., Capaccioni, F., Cerroni, P., Coradini, A., Korablev, O., Kottsov, V., Ignatiev, N., Titov, D., Zasova, L., Pinet, P., Schmitt, B., Sotin, C., Hauber, E., Hoffmann, H., Jaumann, R., Keller, U., Forget, F., 2005. Phyllosilicates on Mars and implications for early martian climate. Nature 438, 623–627. doi:10.1038/nature04274.

Seelos, F., Parente, M., Clark, T., Morgan, F., Barnouin-Jha, O., McGovern, A., Murchie, S.L., Taylor, H., 2009. CRISM hyperspectral data filtering with application to MSL landing site selection, in: AGU Fall Meet., pp. P23A–1234.

Seelos, F.P., Morgan, M.F., Taylor, H.W., Murchie, S.L., Humm, D.C., Seelos, K.D., Barnouin-Jha, O.S., Viviano-Beck, C.E., CRISM Team, 2012. CRISM map projected targeted reduced data records (MTRDRs) – high level analysis and visualization data products, in: Planet. Data A Work. Users Softw. Dev.

Seelos, F.P., Murchie, S.L., Humm, D.C., Barnouin, O.S., Morgan, F., Taylor, H.W., Hash, C., Team, C., 2011. CRISM data processing and analysis products update – calibration, correction, and visualization, in: 42nd Lunar Planet. Sci. Conf., The Woodlands, TX. Abstract no. 1438.

Seelos, F.P., Viviano-Beck, C.E., Morgan, M.F., Romeo, G., Aiello, J.J., Murchie, S.L., 2016. CRISM hyperspectral targeted observation PDS product sets - TERs and MTRDRs, in: 47th Lunar Planet. Sci. Conf., The Woodlands, TX. Abstract no. 1783.

Smith, M.D., Wolff, M.J., Clancy, R.T., Murchie, S.L., 2009. Compact Reconnaissance Imaging Spectrometer observations of water vapor and carbon monoxide. J. Geophys. Res. 114, E00D03. doi:10.1029/2008JE003288.

Tarnas, J.D., Mustard, J.F., Lin, H., Goudge, T.A., Amador, E.S., Bramble, M.S., Kremer, C.H., Zhang, X., Itoh, Y., Parente, M., 2019. Orbital Identification of Hydrated Silica in Jezero Crater, Mars. Geophys. Res. Lett. 46, 12771–12782. doi:10.1029/2019GL085584.

Viviano-Beck, C.E., Seelos, F.P., Murchie, S.L., Kahn, E.G., Seelos, K.D., Taylor, H.W., Taylor, K., Ehlmann, B.L., Wisemann, S.M., Mustard, J.F., Morgan, M.F., 2014. Revised CRISM spectral parameters and summary products based on the currently detected mineral diversity on Mars. J. Geophys. Res. E Planets 119, 1403–1431. doi:10.1002/2014JE004627.

Warren, S.G., 1984. Optical constants of ice from the ultraviolet to the microwave. Appl. Opt. 23, 1206–1225.

Williford, K.H., Farley, K.A., Stack, K.M., Allwood, A.C., Beaty, D., Beegle, L.W., Bhartia, R., Brown, A.J., de la Torre Juarez, M., Hamran, S.E., Hecht, M.H., Hurowitz, J.A., Rodriguez-Manfredi, J.A., Maurice, S., Milkovich, S., Wiens, R.C., 2018. Chapter 11 - The NASA Mars 2020 Rover Mission and the Search for Extraterrestrial Life, in: Cabrol, N.A., Grin, E.A. (Eds.), From Habitability to Life Mars.

Elsevier, pp. 275–308. doi:10.1016/B978-0-12-809935-3.00010-4.

Wiscombe, W.J., 1979. Mie Scattering Calculations–Advances in Technique And Fast, Vector-Speed Computer Codes. NCAR Tech. Note NCAR/TN-140+STR .

Wiseman, S.M., Arvidson, R.E., Wolff, M.J., Smith, M.D., Seelos, F.P., Morgan, F., Murchie, S.L., Mustard, J.F., Morris, R.V., Humm, D., McGuire, P.C., 2016. Characterization of artifacts introduced by the empirical volcano-scan atmospheric correction commonly applied to CRISM and OMEGA near-infrared spectra. Icarus 269, 111–121. doi:10.1016/j.icarus.2014.10.012.

Wolff, M.J., Smith, M.D., Clancy, R.T., Arvidson, R., Kahre, M., Seelos IV, F., Murchie, S., Savijärvi, H., 2009. Wavelength dependence of dust aerosol single scattering albedo as observed by the Compact Reconnaissance Imaging Spectrometer. J. Geophys. Res. E Planets 114, 1–17. doi:10.1029/2009JE003350.

Wright, J., Ma, Y., 2010. Dense error correction via ℓ^1-minimization. IEEE Trans. Inf. Theory 56, 3540–3560. doi:10.1109/TIT.2010.2048473, arXiv:0809.0199.

Wright, J., Yang, A.Y., Ganesh, A., Sastry, S.S., Ma, Y., 2009. Robust face recognition via sparse representation. IEEE Trans. Pattern Anal. Mach. Intell. 31, 210–227. doi:10.1109/TPAMI.2008.79.

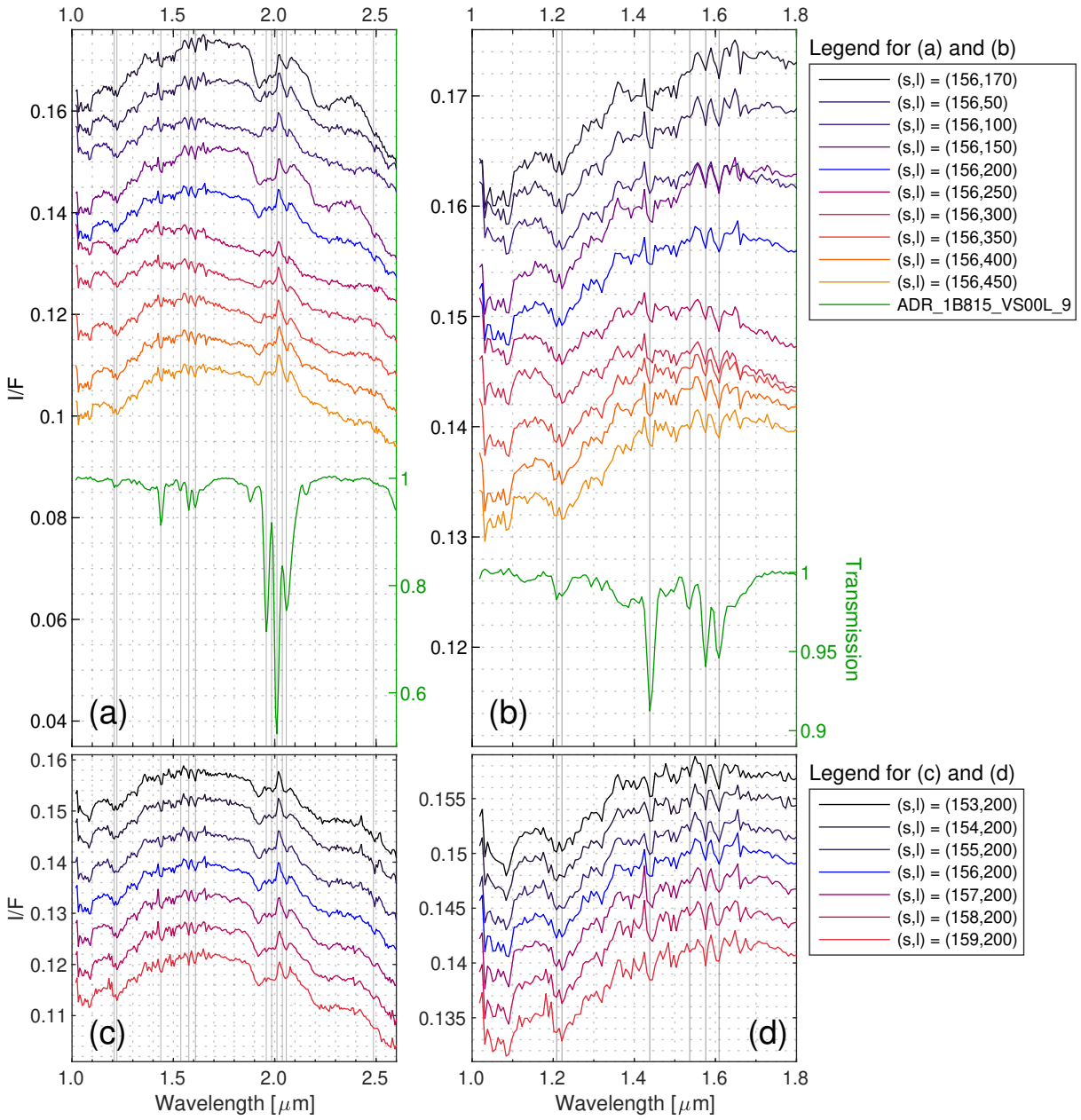

Figure 1: I/F spectra atmospherically corrected using CAT 7.4 on TRR3 data – (a) spectra in column 156 at lines $[170, 50, 100, 150, 200, 250, 300, 350, 400, 450]$ from top to bottom, compared with the transmission spectrum (green) used for correcting these spectra (column 156 in ADR10000000000_1B815_VS00L_9); (b) zoomed version of (a) into the 1.0-1.8 μm wavelength region; (c) spectra in the image frame (200) over several neighboring columns $[153, 154, \ldots, 159]$ from top to bottom; (d) the zoomed version of (c) into the 1.0-1.8 μm wavelength region. All I/F spectra are offset for clarity.

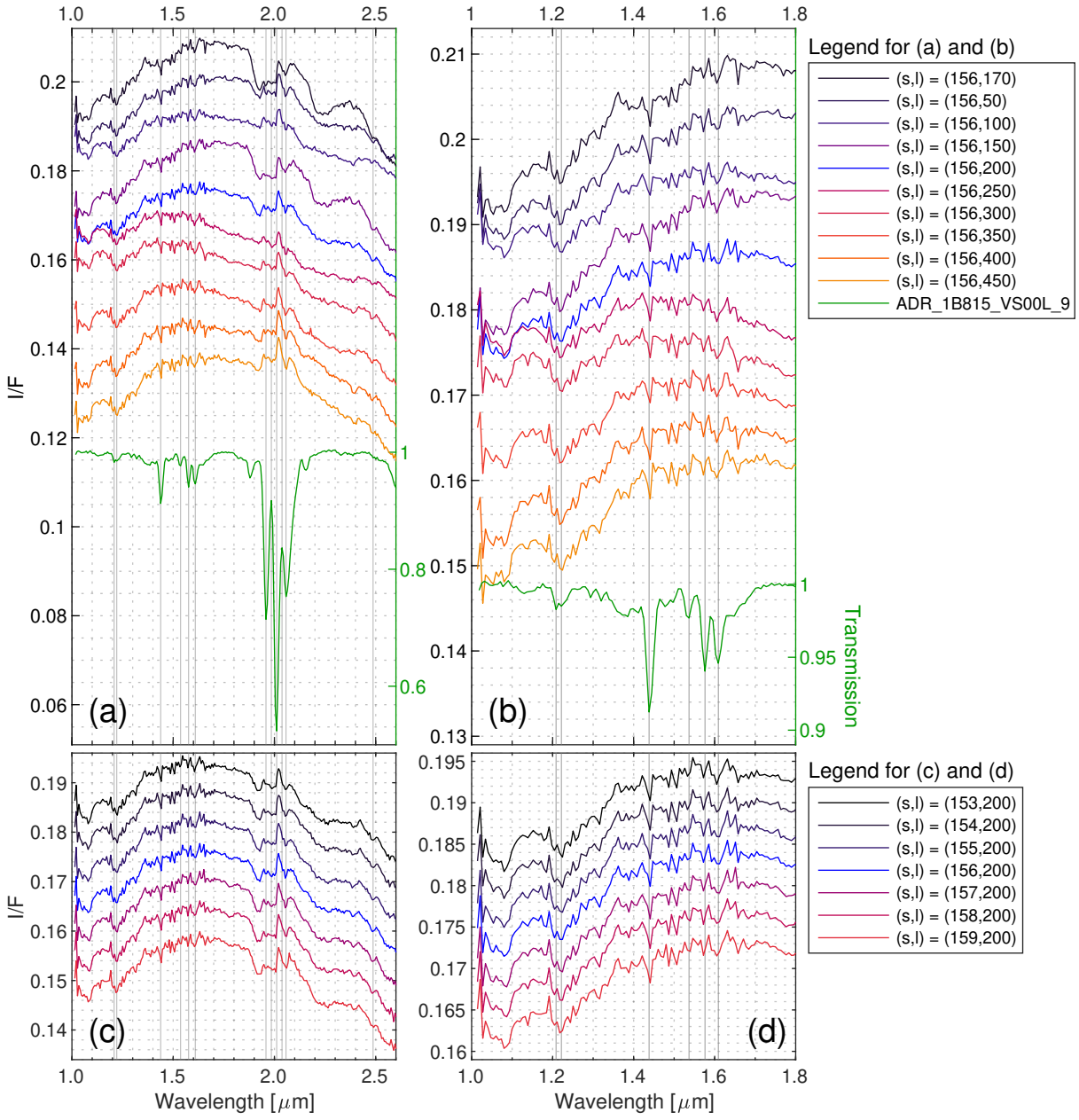

Figure 2: Same comparison as in Fig. 1 of the I/F spectra from the TER product of the observation FRT00009312. Refer to Fig. 1 for an explanation of each panel.

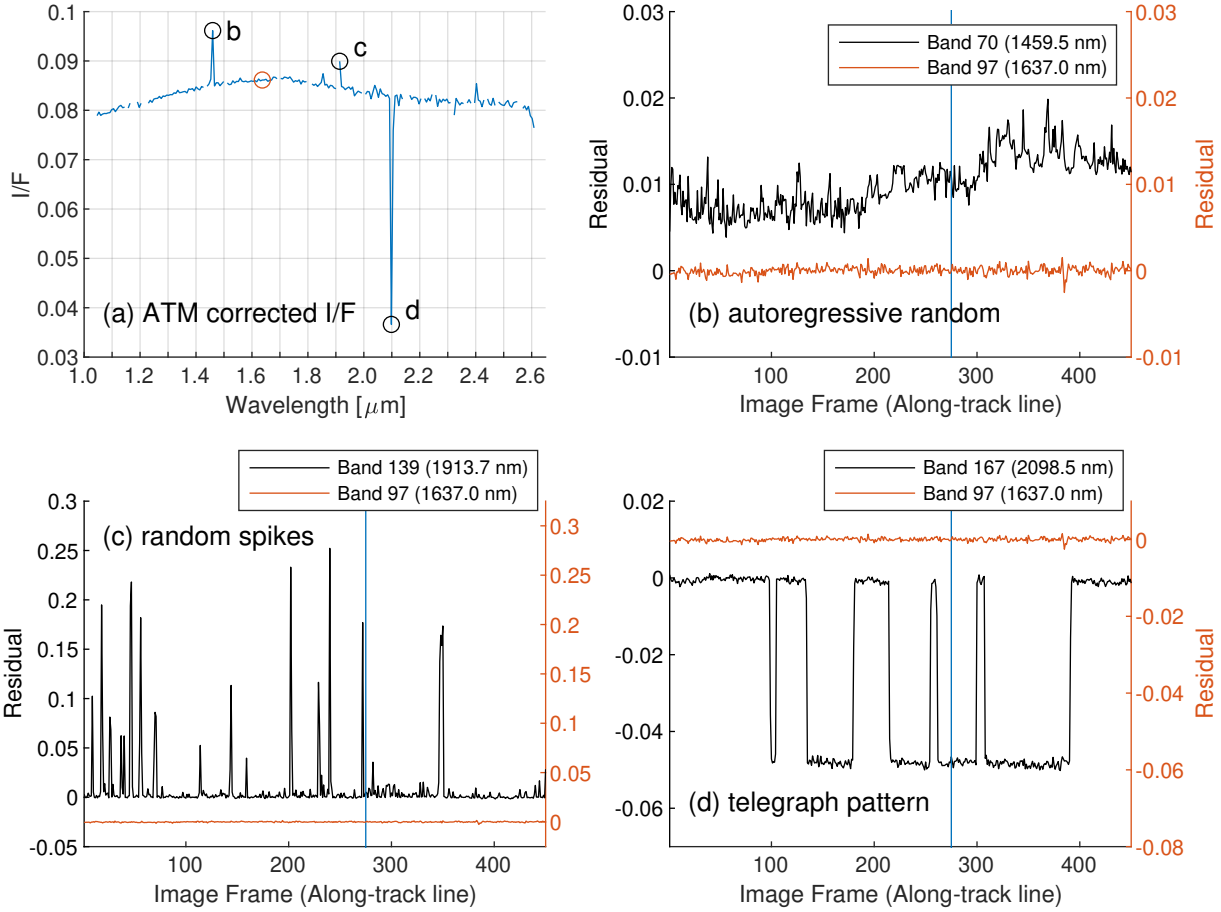

Figure 3: (a) an I/F spectrum atmospherically corrected by our method and (b)-(d) the residual profiles in the along-track direction of some wavelength channels used for the acquisition of the spectrum (a). The spectrum (a) is obtained at the image coordinate (sample, line) of (117,275) in the scene image FRT00024C1A. Black profiles in (b), (c), and (d) are associated with the bands 369 (1459.5 nm), 300 (1913.7 nm), and 369 (2098.5 nm) of the cross-track pixel number 117, respectively, which are supposed to be "bad." The red profiles in (b)-(d) are all from the band 342 (1637 nm), which is supposed to be "good." The black and red circles in (a) are associated with the wavelength channels of the residual profiles. The blue vertical lines in (b)-(d) shows the image frame number where the spectrum (a) is acquired.

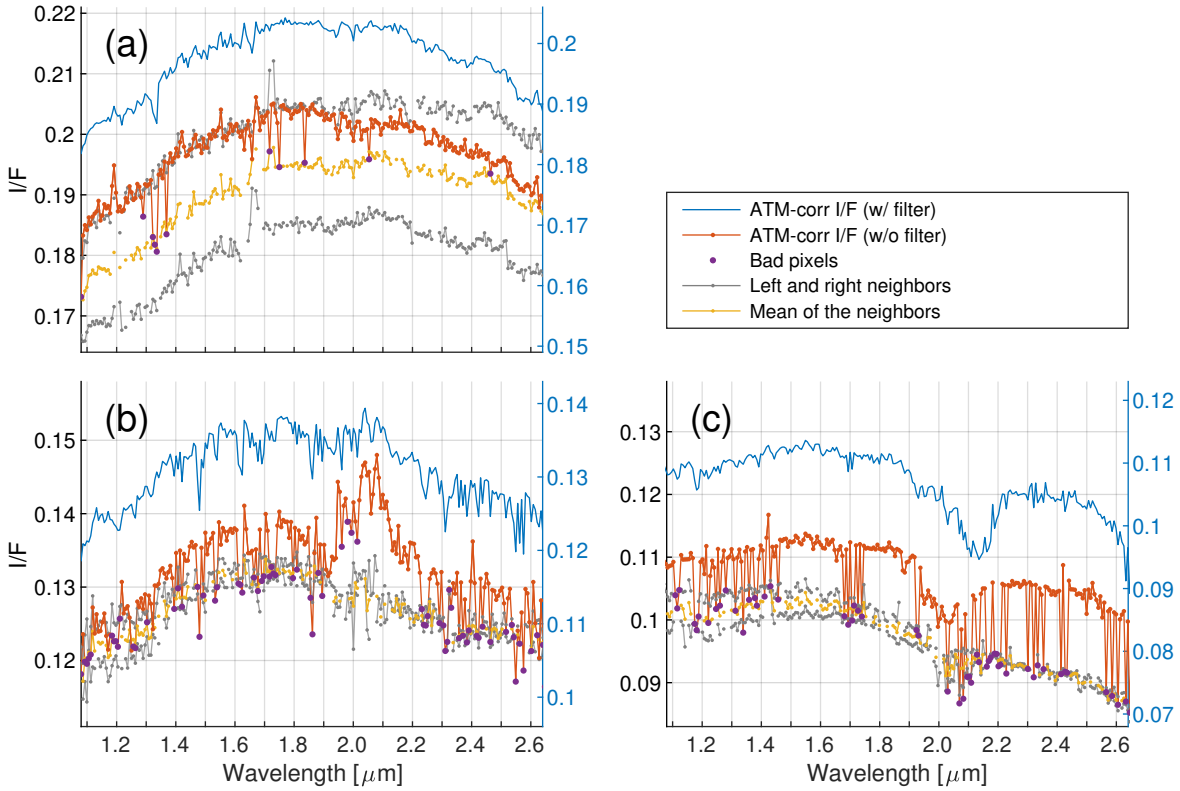

Figure 4: Comparison of non-Filtered I/F spectra atmospherically corrected by CAT (red) with their column neighbors (gray), the mean of column neighbors (yellow), and filtered I/F spectra atmospherically corrected by CAT (blue). The image coordinates (sample, line) of these spectra are (a) (403,172) in FRT0000A546, (b) (386,166) in FRT000174F4, and (c) (90,318) in HRL0000C0BA.

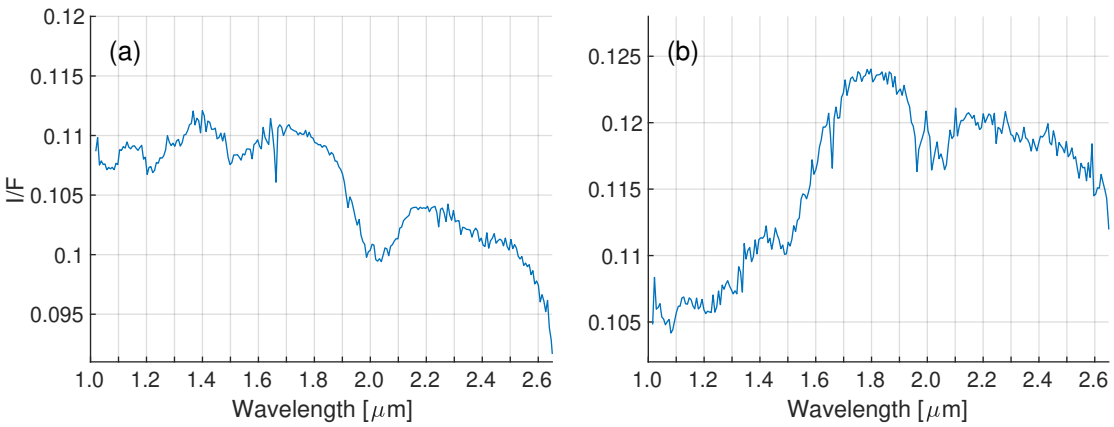

Figure 5: Atmospherically corrected I/F spectra by CAT that exhibit the absorption features of water ice aerosols. Their image coordinates (sample, line) are (a) (597,220) in FRT0000B573 and (b) (247,230) in HRL0002422E.

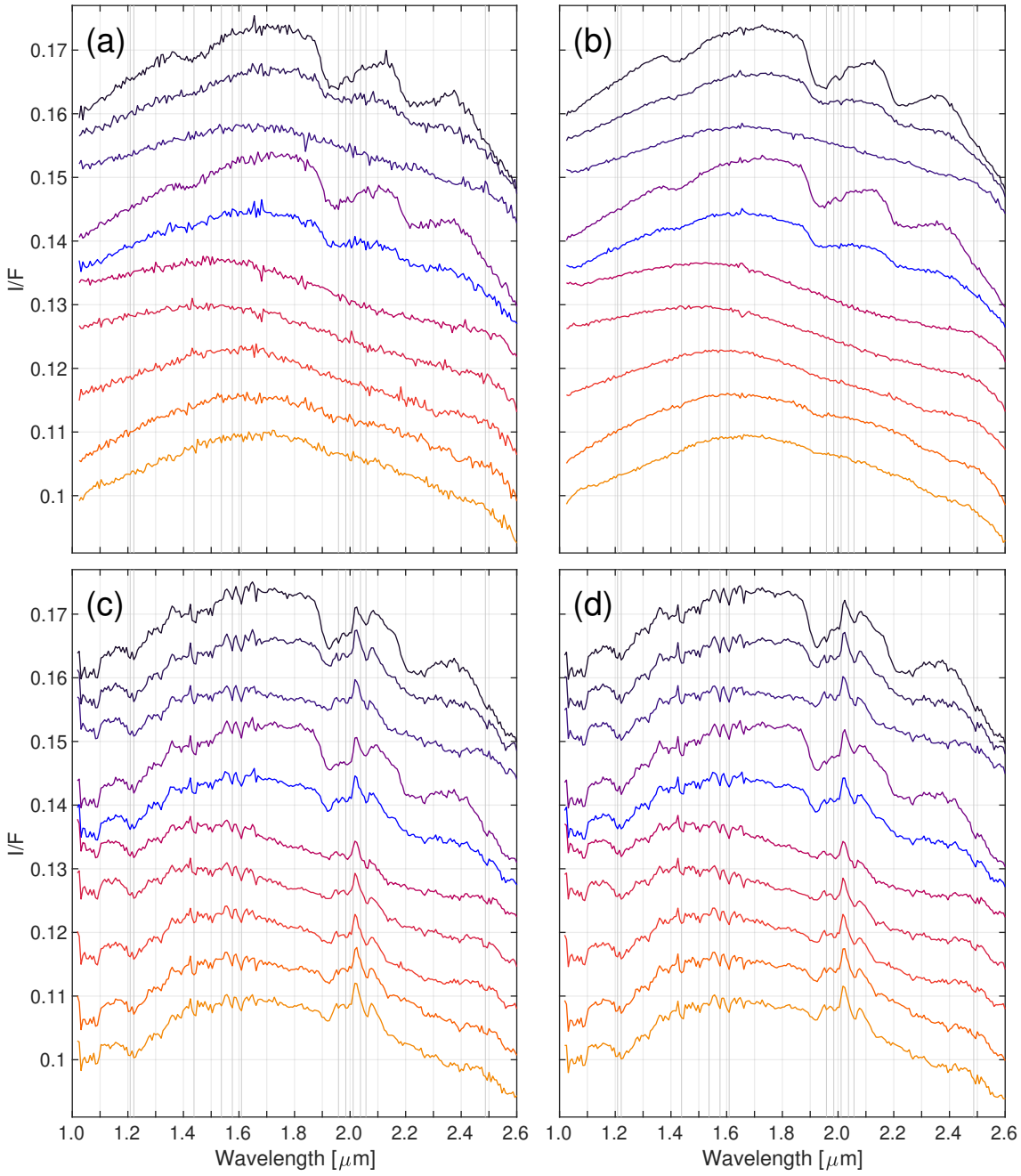

Figure 6: Comparison of I/F spectra atmospherically corrected by our method ((a) and (b)) and ones corrected using CAT 7.4 on TRR3 I/F data ((c) and (d)). (b) and (d) are the 5×5 spatial averages of (a) and (c), respectively. Spectra are in the column (156) in the observation FRT00009312_07 and their image coordinates are identical to the ones in Fig. 1.

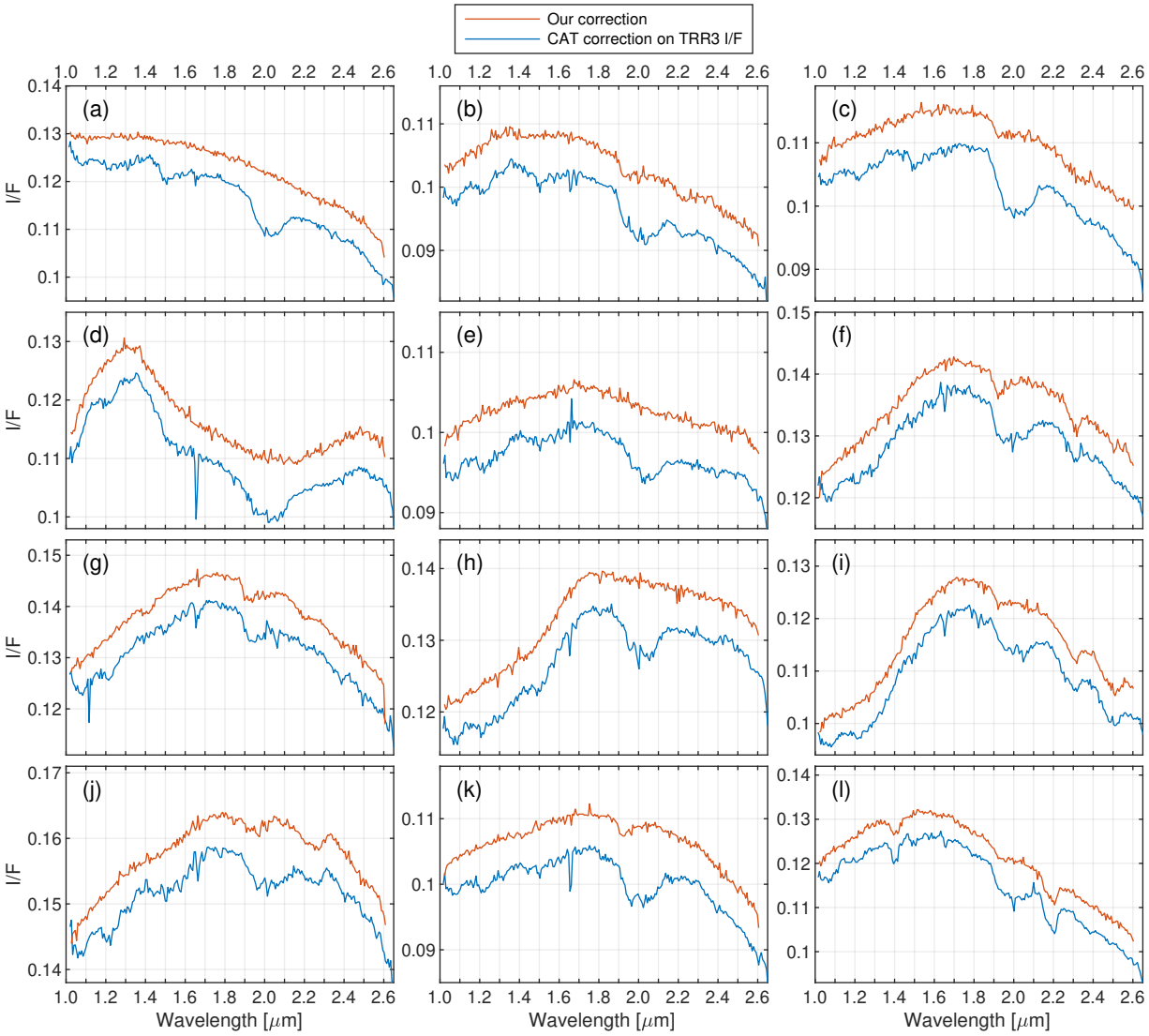

Figure 7: Comparison of I/F spectra atmospherically corrected by our method with water ice (in red) and by CAT (in blue). The spectra (a)-(d) are from FRT0000B573 and their image coordinates (sample, line) are (a) (286, 307), (b) (550,202), (c) (213, 57), and (d) (555,211) respectively. The spectra (e)-(k) are from HRL0000B8C2 and their image coordinates are (e) (289, 122), (f) (149,364), (g) (83,433), (h) (111,415), (i) (138, 61), (j) (313,406), and (k) (276,265) respectively. The spectra (l) are from FRT0000ABCB and their image coordinate is (265,460). The blue spectra are shifted downward for ease of comparison.

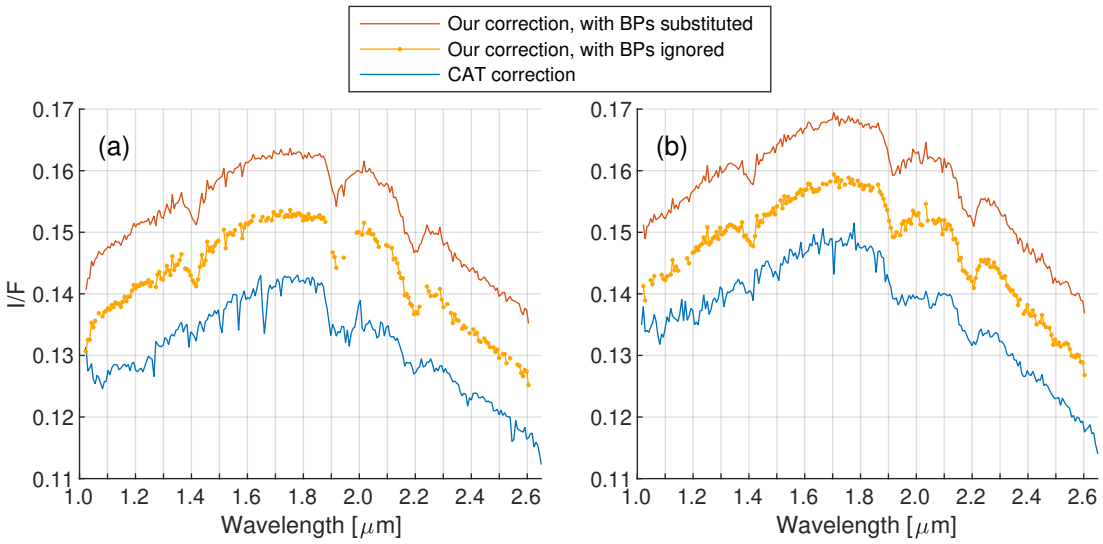

Figure 8: Comparison of I/F spectra atmospherically corrected by our method with (red) or without (orange) bad entries substituted and with CAT on TRR3 I/F (blue) for the same (approximate) location in two overlapping images. (a) Spectra are from (535,016) in FRT000174F4 and (b) Spectra are from (276,432) in FRT0001821C. Spectra are shifted for ease of comparison.

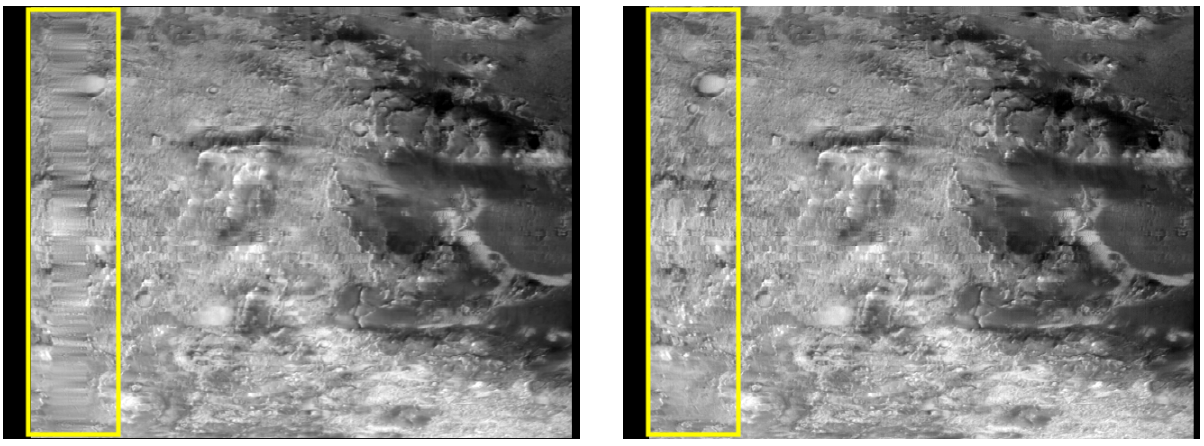

(a) (b)

Figure 9: Comparison of two band images corrected with our method (a) and with CAT on filtered I/F (b). They are the band 302 (1.895μm) of FRT0001821C.

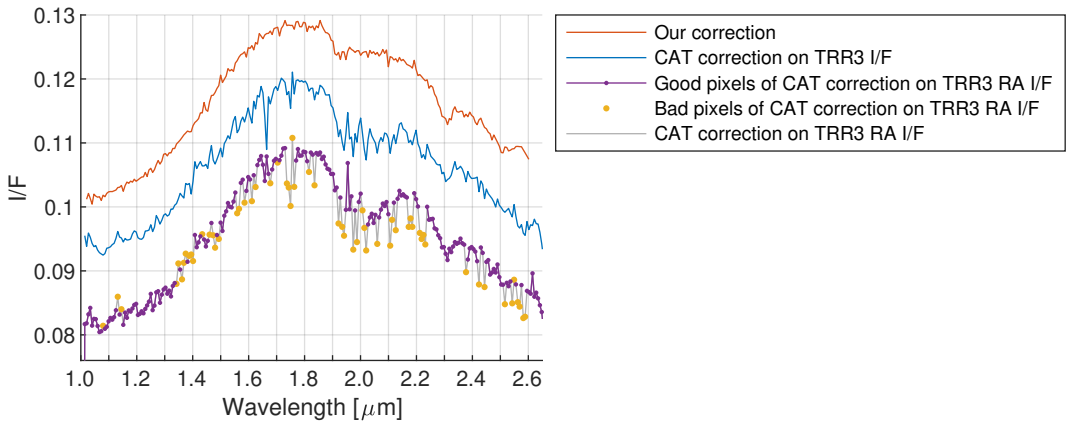

Figure 10: Comparison of I/F spectra corrected with our method (red) with those corrected with CAT on TRR3 I/F (blue) and with CAT on TRR3 I/F without filtering (gray/purple/yellow). Yellow dots represent bad channels (BPs). Purple dots represent non corrupted channels (non-BP). The image coordinate (sample line) of the spectrum is (191,359) in HRL0002422E. Spectra are shifted for ease of comparison.

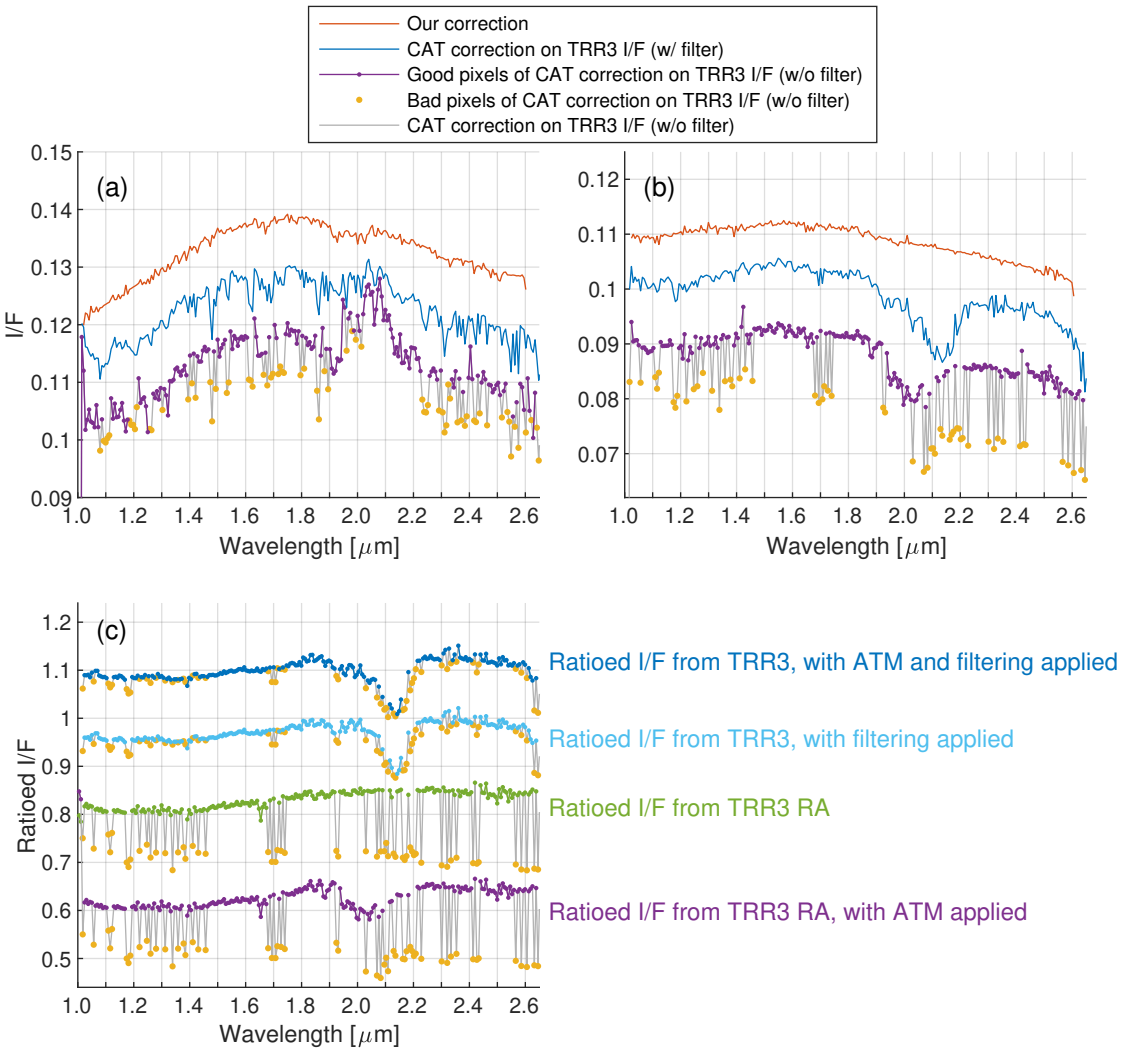

Figure 11: (a-b) Comparison of I/F spectra corrected with our method (red) with those corrected with CAT on TRR3 I/F (blue) and with CAT on TRR3 I/F without filtering (gray/purple/yellow). Yellow and purple dots represent bad channels (BPs) and non-BPs, respectively. (a) and (b) are from (386,166) in FRT000174F4 and from (90,318) in HRL0000C0BA, respectively. Spectra are shifted for ease of comparison. (c) Comparison of the ratioed I/F spectra performed in different ways. From the top to bottom, a ratioed spectrum of filtered I/F atmospherically corrected by CAT (blue), a ratio of filtered I/F (light blue), a ratio of non-filtered I/F (green), and a ratio of non-filtered I/F atmospherically corrected by CAT (purple). These colors are only given for non-BPs. Yellow dots represent BPs for each plot and the whole spectra are plotted in gray. The image coordinate of these spectra is same as that of (b). Spectra are offset for ease of comparison.

.

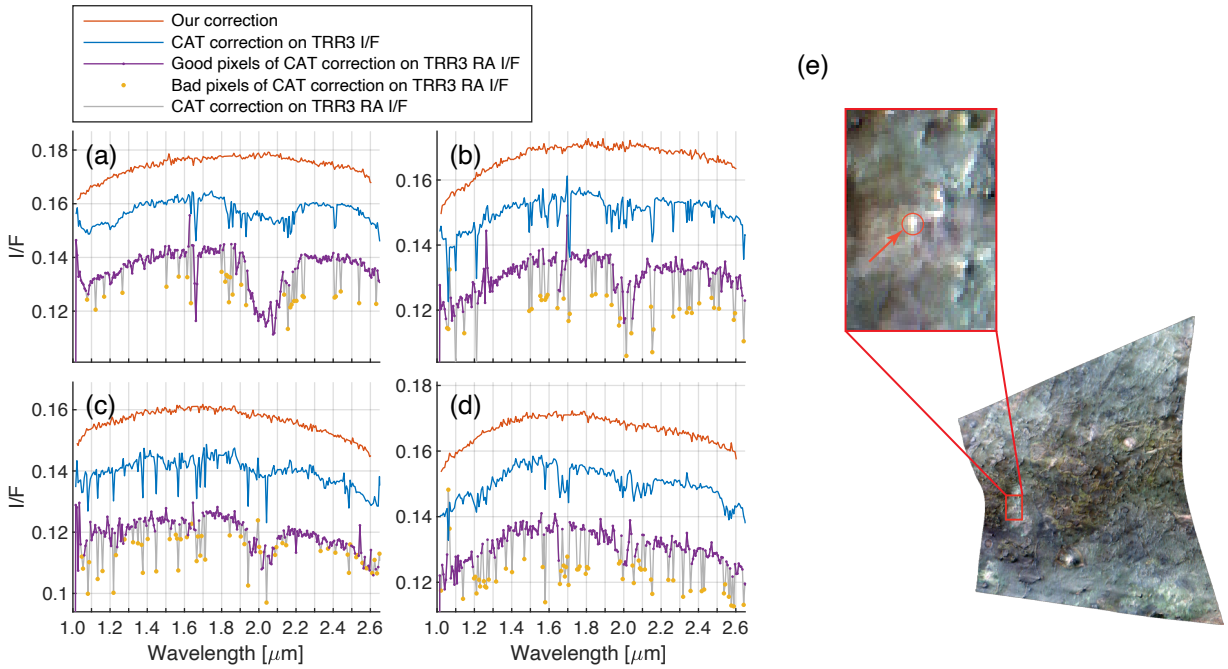

Figure 12: Comparison of I/F spectra corrected with our method (red) with those corrected with CAT on TRR3 I/F (blue) and with CAT on TRR3 I/F without filtering (gray/purple/yellow). Yellow dots represent bad channels (BPs). Purple dots represent non corrupted channels (non-BP). Spectra in (a), (b), (c), and (d) are from (552,209) in FRT000161EF, (294,163) in FRT000174F4, (474,190) in FRT00018781, and (295,119) in FRT00017103, respectively. The blue and purple spectra are shifted downward for ease of comparison. (e) a pseudo RGB map-projected image of FRT000161EF with a zoomed-in image into a location associated with the spectra.

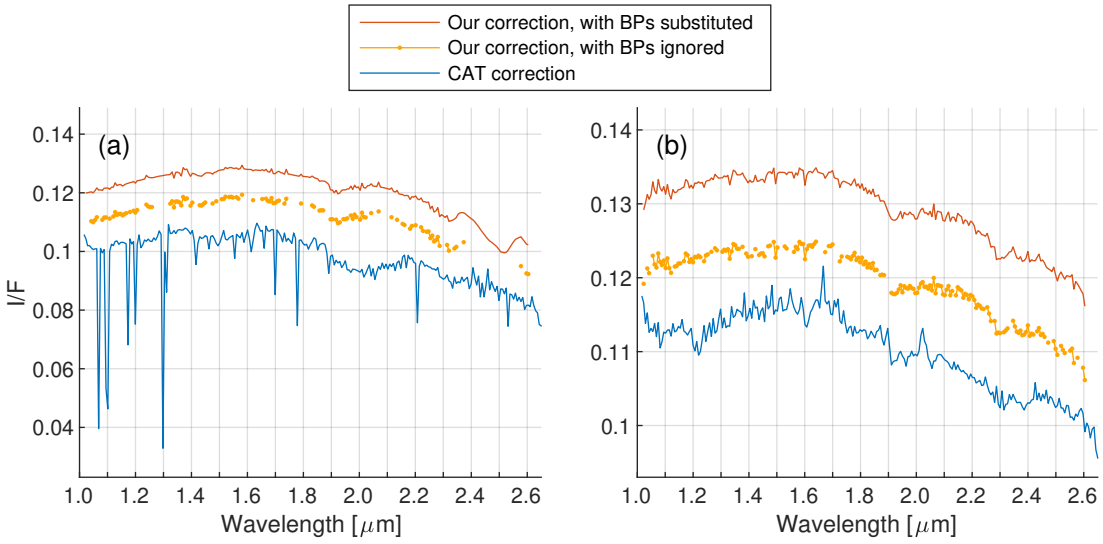

Figure 13: Comparison of I/F spectra atmospherically corrected by our method with (red) or without (orange) bad entries substituted and corrected with CAT on TRR3 I/F (blue). Spectra are from (a) (255,270) in FRT000243C0 and (b) (518,126) in FRS00029DA6. Spectra are shifted for ease of comparison.

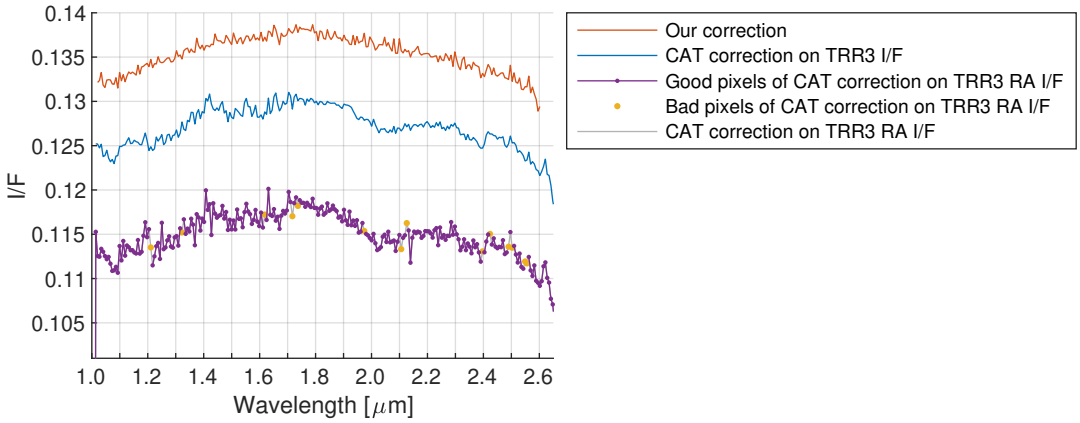

Figure 14: Comparison of I/F spectra corrected with our method (red) with those corrected with CAT on TRR3 I/F (blue) and with CAT on TRR3 I/F without filtering (gray/purple/yellow). Yellow dots represent bad channels (BPs). Purple dots represent non corrupted channels (non-BP). Spectra are from (391,449) in FRT00003192. Spectra are shifted for ease of comparison.

Supplemental material for "A new method for atmospheric correction and de-noising of CRISM hyperspectral data"

Yuki Itoh[a], Mario Parente[a]

[a]*Department of Electrical and Computer Engineering, University of Massachusetts, Amherst*

Summary: This supplemental document provides additional examples of comparison with our approach.

Fig. S1 shows additional comparisons from FRT000174F4. Our method still produces cleaner spectra, while the blue spectra are corrupted by atmospheric residuals and artifact due to interpolation bias. Fig. S2 (a) shows the comparison of I/F spectra corrected by our method and CAT (identical to Fig. 11 (c) in the main text) and Fig. S2 (b) shows ratioed I/F spectra of the same pixel processed in the four different approaches. In Fig. S2, our corrected spectrum (red) is bland, while CAT correction creates a big depression around the 2.0 μm wavelength region whether or not TRR3 filtering is applied or not. Fig. S2 (b) shows that the depression present in I/F spectra corrected with CAT is an artifact. The ratioed filtered I/F (darker blue) with atmospheric correction exhibits a depression right at 2.0 μm while the ratioed filtered I/F (light blue) without atmospheric correction does not, indicating the center of the depression around 2.0 μm is likely to be an artifact caused by atmospheric correction. The 1.9 and 2.1 μm absorptions in the light blue spectrum are likely to be caused by interpolation bias because the absorptions are not observed in the ratioed non-filtered I/F (green) without atmospheric correction and BPs with moderate interpolation bias are concentrated around these wavelength regions. These 1.9 and 2.1 μm artifacts are likely to be identical to problematic *spurious features* reported in (Leask et al., 2018). Therefore, we can conclude that the combination of these artifacts – the bow-shape one around at 2.0 μm and the spurious features at 1.9 and 2.1 μm – ends up in a broad depression around 2.0 μm in the blue spectrum in Fig. S2 (a).

Figs. S3 and S4 show another comparison of the spectra at the same location measured

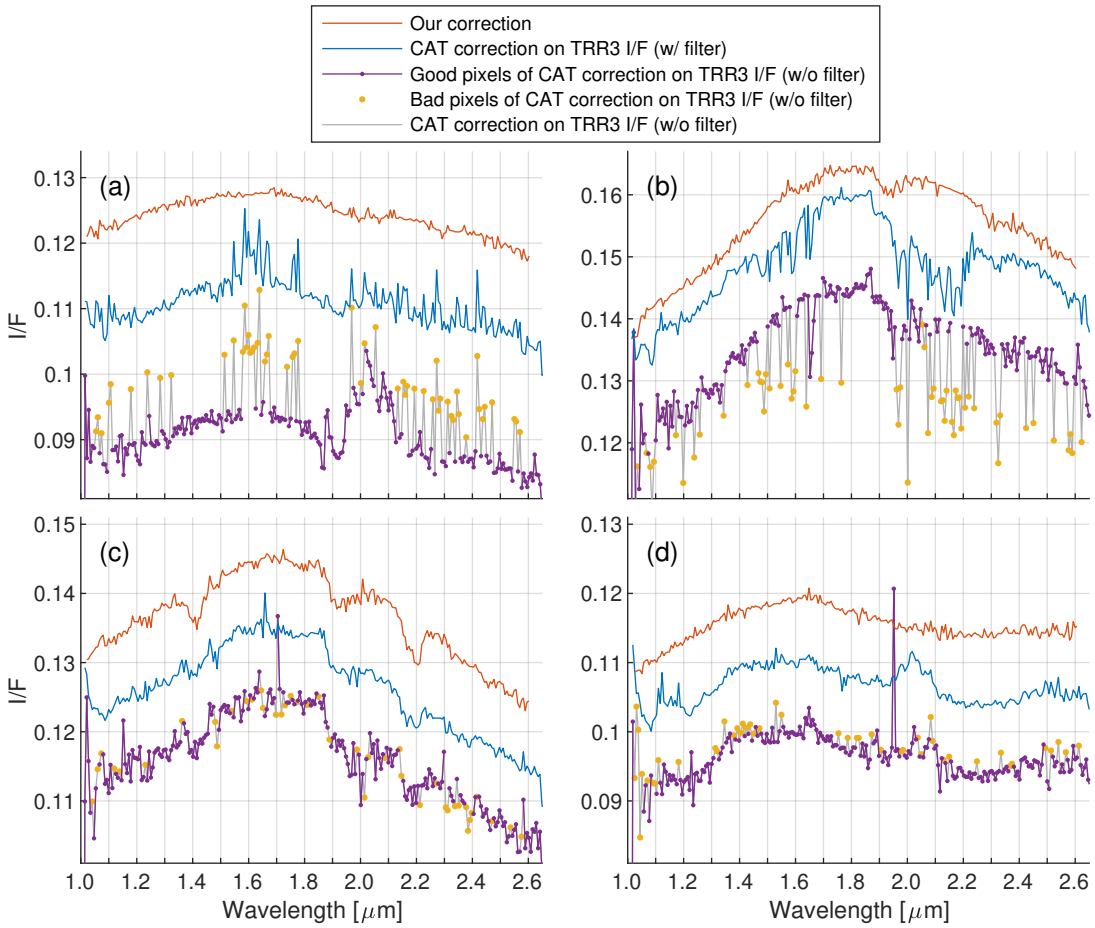

Figure S1: Comparison of I/F spectrum corrected with our method (red) with those corrected with CAT on TRR3 I/F (blue) and with CAT on TRR3 I/F without filtering (gray/purple/yellow). Yellow dots represent bad channels (BPs). Purple dots represent non corrupted channels (non-BP). Spectra in (a), (b), (c), and (d) are from (270,172), (269,194), (426, 15), and (161,170) in FRT000174F4, respectively. Spectra are offset for ease of comparison.

in different images. Those are inside the final candidate landing ellipses for 2020 Mars Rover in North East Syrtis and in Jezero crater. Fig. S3 shows that Mg/Fe-carbonate features are seen on all the images. The interpolation bias is less problematic on those spectra because the unit spans 10 or more pixels around it. In contrast, the spectra in Fig. S4 shows smaller features. For different images, 1.9 and 2.3 μm absorptions are consistently seen, although those of (b) and (c) are quite small and the continua of the spectra look different. Such a difference may happen partly because those locations do not match perfectly and have subpixel shifts, or because of the different conditions of dust aerosols.

Finally, we compare spectra corrected by our method and corrected by CAT at some locations of particular interest reported in the literature. Fig. S5 shows the comparison of the spectra at the locations reported in (Bramble et al., 2017) processed by our proposed method and by the volcano scan correction using CAT. The spectra shown in the figure are averaged within the same spatial windows provided in a supplemental table file in Bramble et al. (2017). Our method produces spectral shapes comparable to ratioed spectra without ratioing, while non-ratioed CAT-corrected spectra exhibit more noise and artifacts. The comparison of ratioed spectra also shows that our method removes some of the spiky noise, such as 1.2 μm in the ratio of CAT-corrected spectrum in Fig. S5 (a) and 1.65 and 1.9 μm in the ratio of CAT-corrected spectrum in Fig. S5 (d). A remaining concern would be our corrected spectra show slightly smaller absorption bands in the ratioed spectra. Another concern would be that our corrected spectra sometimes become unrealistically angular. For instance, the denominator spectrum of (a) jarosite shows an angular shape around 1.65 μm.

References

Bramble, M.S., Mustard, J.F., Salvatore, M.R., 2017. The geological history of Northeast Syrtis Major, Mars. Icarus 293, 66–93. doi:10.1016/j.icarus.2017.03.030.

Leask, E.K., Ehlmann, B.L., Dundar, M.M., Murchie, S.L., Seelos, F.P., 2018. Challenges in the search for perchlorate and other hydrated minerals With 2.1-μm absorptions on Mars. Geophys. Res. Lett. 45, 12,180–12,189. doi:10.1029/2018GL080077.

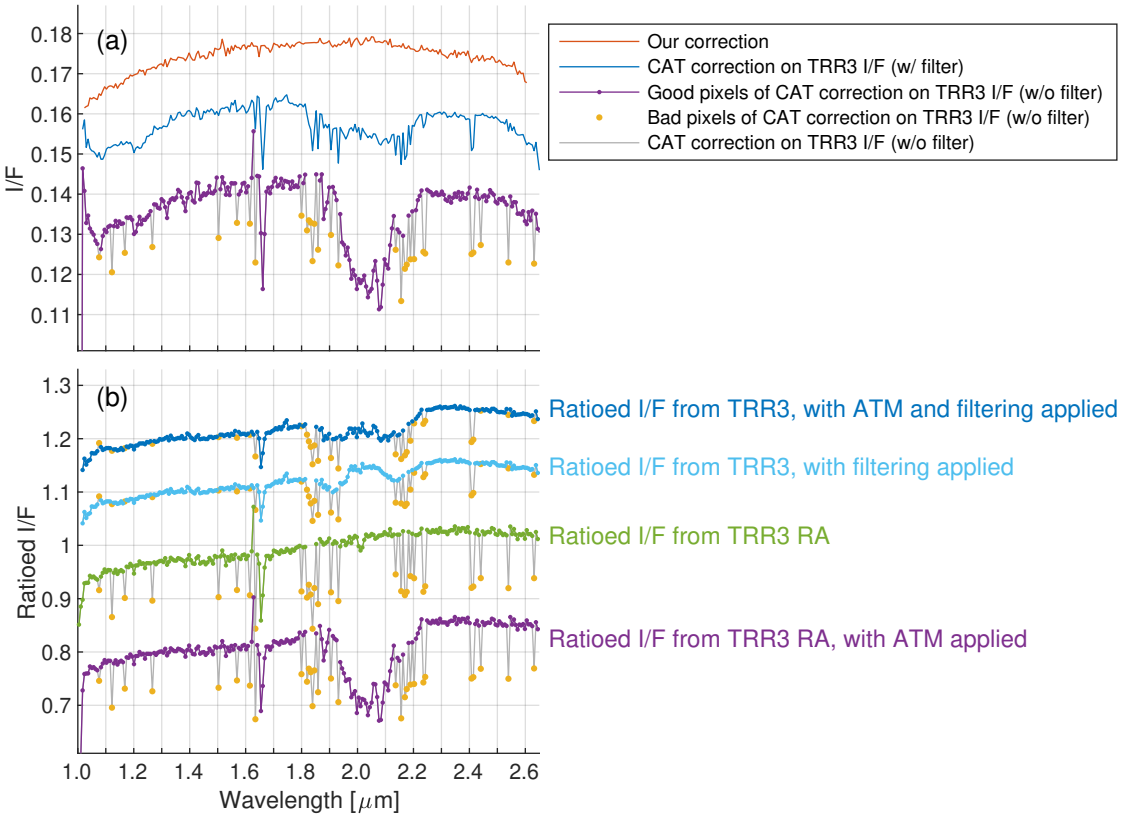

Figure S2: (a) Comparison of I/F spectra corrected with our method (red) with those corrected with CAT on TRR3 I/F (blue) and with CAT on TRR3 I/F without filtering (gray/purple/yellow). Yellow dots represent bad channels (BPs). Purple dots represent non corrupted channels (non-BP). Spectra are from (552,209) in FRT000161EF (same as Fig. 12 (a) in the main text). The blue and purple spectra are shifted downward for ease of comparison. (b) Comparison of the ratioed I/F spectra performed in different ways. From the top to bottom, a ratioed spectrum of filtered I/F atmospherically corrected by CAT (blue), a ratio of filtered I/F (light blue), a ratio of non-filtered I/F (green), and a ratio of non-filtered I/F atmospherically corrected by CAT (purple). These colors are only given for non-BPs. Yellow dots represent BPs for each plot and the whole spectra are plotted in gray. Spectra are shifted for ease of comparison.

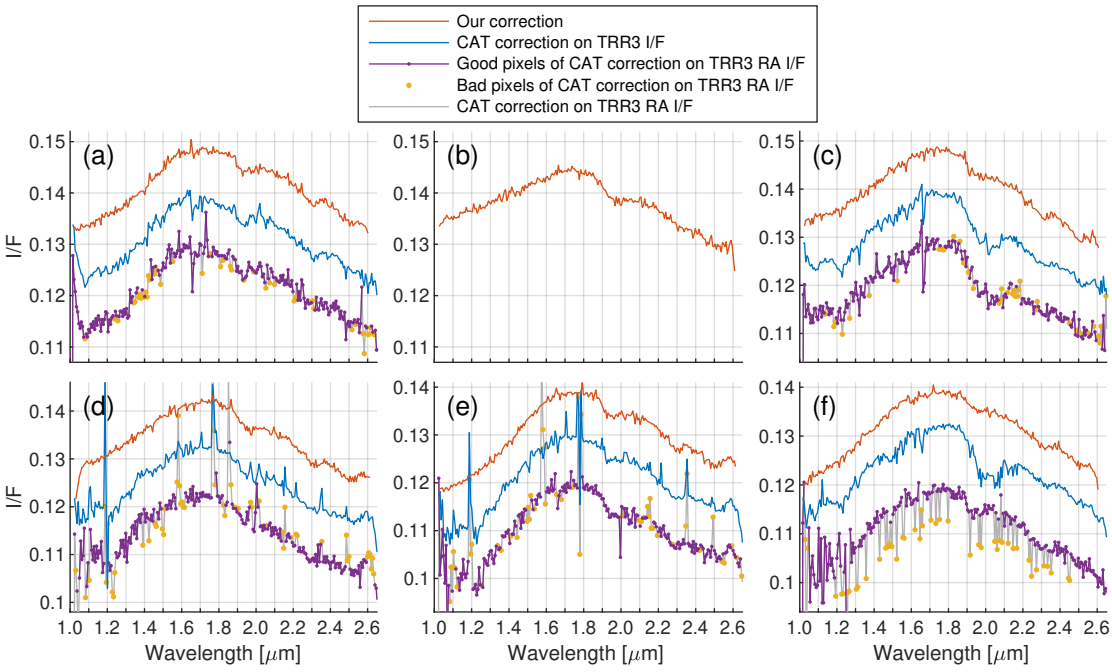

Figure S3: Comparison of I/F spectra corrected with our method (red) with those corrected with CAT on TRR3 I/F (blue) and with CAT on TRR3 I/F without filtering (gray/purple/yellow). Yellow dots represent bad channels (BPs). Purple dots represent non corrupted channels (non-BP). They are from (a) (342,231) in FRT000161EF, (b) (632,190) in FRT0001642E, (c) (604,177) in FRT000165F7, (d) (46,127) in FRT00017103, (e) (43, 180) in FRT000174F4, and (f) (217,207) in FRT00018781. The blue and purple spectra are shifted downward for ease of comparison.

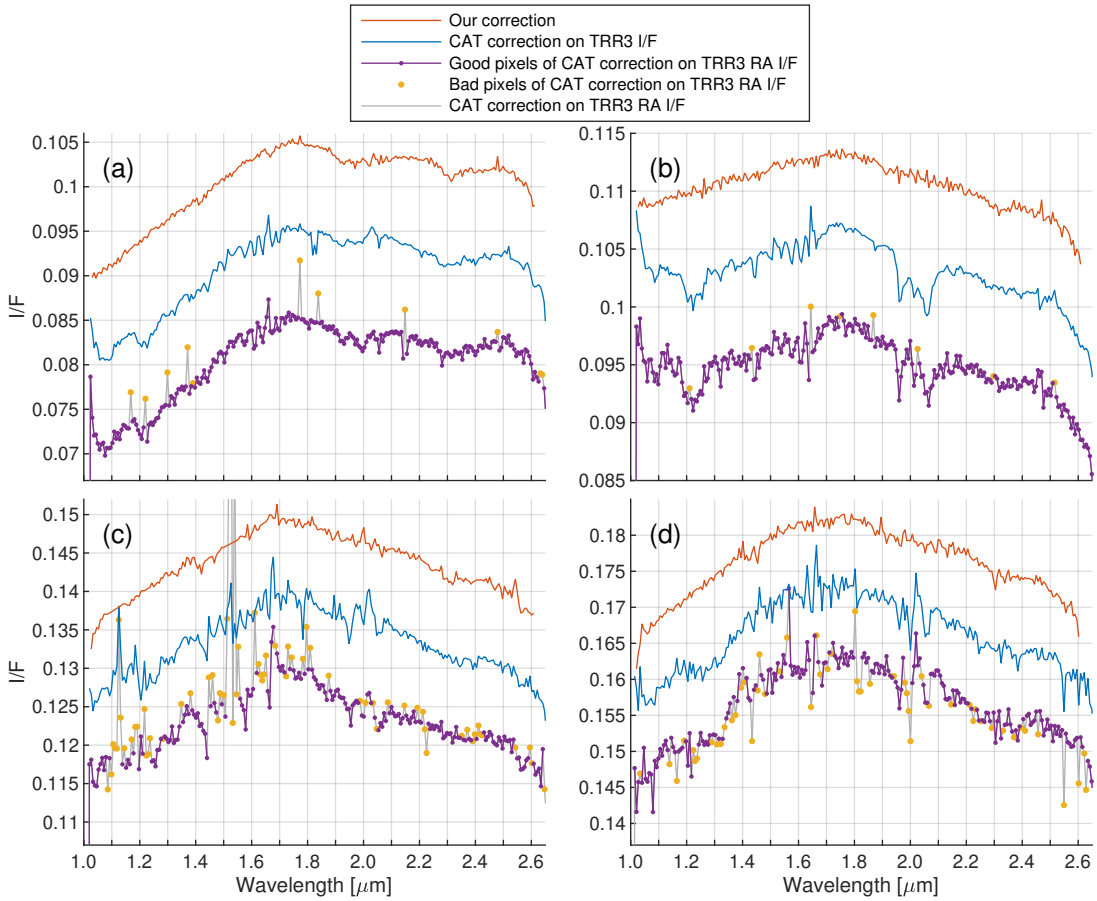

Figure S4: Comparison of I/F spectra corrected with our method (red) with those corrected with CAT on TRR3 I/F (blue) and with CAT on TRR3 I/F without filtering (gray/purple/yellow). Yellow dots represent bad channels (BPs). Purple dots represent non corrupted channels (non-BP). Spectra in (a), (b), (c), and (d) are from (25,154) in HRL000040FF, (115, 42) in FRT00005C5E, (623,460) in FRT0001EAE0, and (360,472) in FRT0001FB74, respectively. The blue and purple spectra are shifted for ease of comparison.

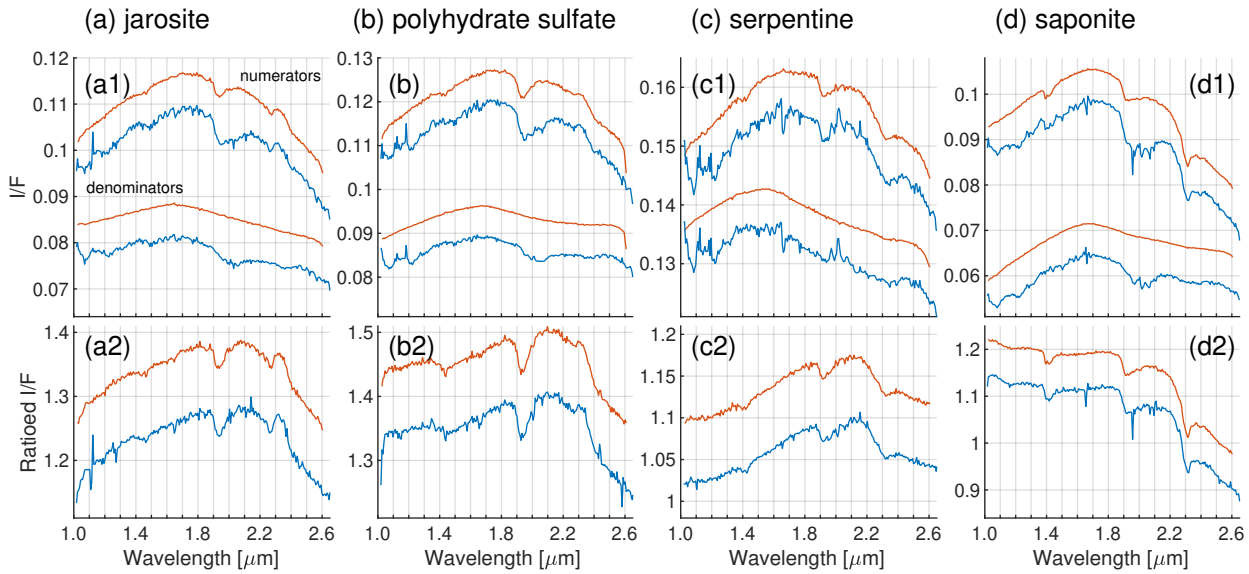

Figure S5: Comparison of atmospherically corrected I/F spectra and ratioed spectra corrected by our method (red) and by volcano scan using CAT on TRR3 filtered I/F (blue) of (a) jarosite, (b) polyhydrated sulfate, (c) serpentine, and (d) saponite. (a1)-(d1) are the comparisons of I/F spectra and (a2)-(d2) are those of ratioed I/F spectra. In (a1)-(d1), the two upper spectra (red and blue) are numerators and the two lower ones are denominators (red and blue). Spectra are shifted for ease for comparison. Their image coordinates and spatial average sizes are reported in Bramble et al. (2017).